This is a non-peer-reviewed preprint submitted to EarthArXiv.

The manuscript has also been submitted to *Engineering Geology* and has not yet been peer reviewed. Later versions may differ. If the paper is accepted, the published version will be linked from the EarthArXiv page of this preprint.

Post-event information in calendar-year satellite products inflates landslide susceptibility assessments

Yifan Du* https://orcid.org/0009-0008-7740-5408
Tianhe Zheng https://orcid.org/0009-0000-8993-814X
Peiyan Yang https://orcid.org/0009-0004-6214-0831
Yibo Li https://orcid.org/0009-0002-2926-757X
Junhang Zhou https://orcid.org/0009-0002-0458-2127
Kun Yang https://orcid.org/0009-0006-6609-219X

North China University of Water Resources and Electric Power, 136 Jinshui East Road, Zhengzhou 450046, Henan, China

*Corresponding author: Yifan Du, duyifan619916@gmail.com

Code, analysis log and derived data: https://doi.org/10.5281/zenodo.23467612

EarthArXiv accepts a single PDF, so the supplementary material (Texts S1–S6 and Tables S1–S18, pages S1–S20) follows the references. Supplementary Data S1 and S2 are the files `derived_data/v3/aef_manifest.csv` and `derived_data/v3/tessera_manifest.csv` of the Zenodo record above.

Post-event information in calendar-year satellite products inflates landslide susceptibility assessments

Yifan Du[a,*], Tianhe Zheng[a], Peiyan Yang[a], Yibo Li[a], Junhang Zhou[a], Kun Yang[a]

[a]*North China University of Water Resources and Electric Power, 136 Jinshui East Road, Zhengzhou, 450046, Henan, China*

Abstract

Annual satellite products, such as the AlphaEarth Foundations and TESSERA embeddings, summarize a calendar year, so the product of a landslide's event year also contains post-event observations. We audited this post-event information in 18 dated events (7 earthquakes, 11 rainstorms; 61,402 landslides), changing only the input year within each event and keeping the points, spatial folds, models and bootstrap clusters fixed. Replacing the prior-year AlphaEarth product with the event-year product raised the out-of-fold AUC by 0.087 (95% CI 0.065–0.110; all 18 events) for a point model and by 0.071 (0.048–0.093) for a patch CNN. The point-model gain was 0.085 after subtracting each event's drift between two pre-event years. On complete maps, the event-year input added on average 0.21–0.22 of the landslide area to the map's top 10% (9 of 9 events; up to 0.46). A training-year × prediction-year decomposition traced the inflation to models that learn the event's surface changes, chiefly its landslide scars; event-year inputs used only at prediction did not inflate within-event scores on average. The inflation grew with the post-event fraction of the year, reaching half its full size when 23–39% of the year followed the event; this relation survived corrections for recovery. TESSERA and plain Sentinel-2 composites behaved alike. In forward tests in three regions, models trained on earlier landslides scored 0.02–0.11 higher AUC on the new event with event-year inputs, whereas legitimate pre-event embeddings helped mainly near earlier landslides. Susceptibility zoning should use only products whose year ends before the event.

Keywords: landslide susceptibility zoning, model validation, temporal leakage, satellite embeddings, geospatial foundation models, AlphaEarth Foundations

1. Introduction

Landslide susceptibility models estimate where slopes are likely to fail; they are calibrated on mapped landslides, with predictors that describe terrain, land cover,

*Corresponding author.
Email address: duyifan619916@gmail.com (Yifan Du)

lithology and climate (Reichenbach et al., 2018). Susceptibility zoning is one of the zoning products recommended for land-use planning (Fell et al., 2008), and it is increasingly produced with machine-learning models (Merghadi et al., 2020), so the way these models are tested decides how far their maps can be trusted. Work on validation has concentrated on space. Brenning (2005) showed that non-spatial resampling overstates the predictive skill of landslide models when samples are spatially dependent, and spatially separated cross-validation is now widely recommended (Roberts et al., 2017; Ploton et al., 2020; Karasiak et al., 2022). Testing a model on landslides that occurred after those used to build it was proposed early (Guzzetti et al., 2006), but it remains rare: almost all susceptibility studies split a single event or historical inventory into training and test sets (Lombardo and Tanyas, 2020).

Much less attention has gone to the time at which each predictor was observed. A predictor observed after the landslides it is meant to predict carries information that no forecaster would have had, which machine learning calls leakage and recognizes as a common source of over-optimistic results (Kaufman et al., 2012; Kapoor and Narayanan, 2023). In landslide research, the closest precedent concerns topography, since elevation models acquired after failure partly encode the failures (Steger et al., 2020).

The question has become practical with the annual embedding products of geospatial foundation models. AlphaEarth Foundations provides one 64-dimensional vector per 10 m pixel and calendar year, learned from optical, radar and other observations (Brown et al., 2025), and TESSERA provides 128-dimensional annual representations learned from Sentinel-1 and Sentinel-2 time series (Feng et al., 2025). Because both are global and freely available, they were quickly adopted for landslide mapping and susceptibility (Cheng et al., 2026; Fang et al., 2026; Li et al., 2026; Liu et al., 2026) and for other hazards (Knezevic et al., 2026; Thasma et al., 2026; Zhuang et al., 2026). An annual product cannot be cut at an event date. When a study models an event with the product of the event year, the model sees the weeks or months after the event, including the scars, deposits and other surface changes that it is supposed to anticipate.

How common this practice is remains unclear. Of the studies in a small survey that used annual embeddings as predictors of dated hazards, four reported their input years clearly enough to check (Supplementary Text S2). Three of them used embeddings that included the event year or later years (Cheng et al., 2026; Li et al., 2026; Zhuang et al., 2026), and two of these three described the temporal match between embeddings and inventory as an advantage. Only Fang et al. (2026) used the previous year throughout. A flood-mapping study, by contrast, deliberately used embeddings from years long after its events to avoid event leakage (Thasma et al., 2026). The same aggregation effect appears in burned-area mapping, where annual embeddings detect late-year fires less well because few post-fire weeks fall within the aggregation window (Knezevic et al., 2026).

A quantitative account for susceptibility assessment is still missing. This study asks how much event-year inputs inflate common evaluation designs relative to a

placebo, and through which part of the modelling workflow the inflation enters. It also asks whether the inflation depends on when in the year the event occurred, whether it is specific to foundation-model embeddings, and whether it changes the maps and forward predictions that practitioners use.

We address these questions with a strictly paired year swap in 18 dated landslide events (Fig. 1). Within each event, the same points, folds, bootstrap clusters and models are evaluated with annual inputs from two years before to two years after the event, so that differences between years can be attributed to the input year alone. We then split the inflation into its training and prediction parts and relate it to the post-event fraction of the calendar year, with explicit checks for recovery. The audit is then repeated with a second embedding product and with plain Sentinel-2 composites, extended to complete maps, and complemented by forward tests in three regions. The design and decision criteria of every analysis were written into a time-stamped analysis log before computation, and we report the tests that failed together with those that passed.

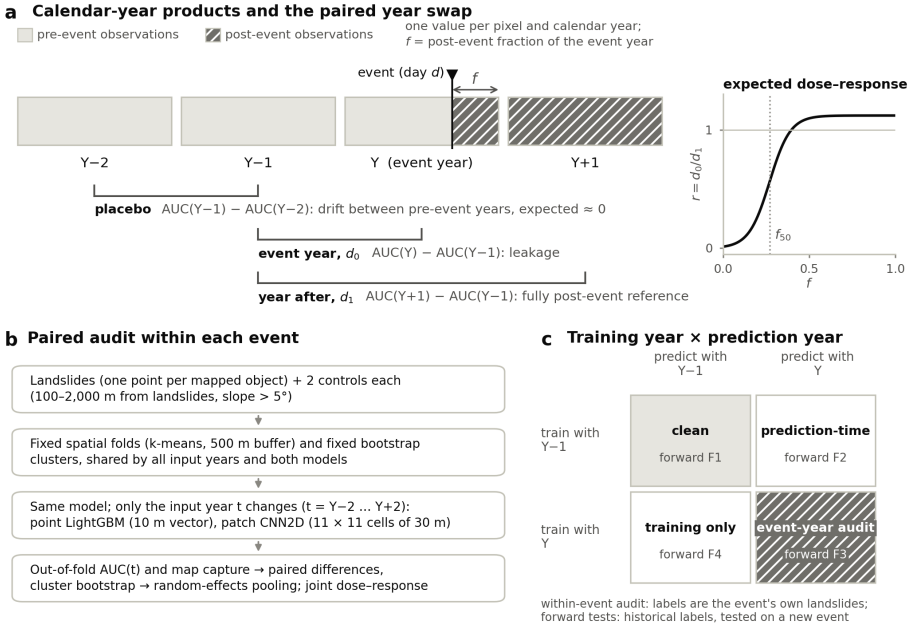


Fig. 1. Study design. (a) Annual products summarize one calendar year. For an event on day d of year Y, the event-year product contains a post-event fraction $f = (365 - d)/365$ of the year. The paired year swap compares out-of-fold AUCs of the same model with inputs from different years. The contrasts are the event-year increment d_0 (Y vs Y−1), the placebo (Y−1 vs Y−2) and the year-after increment d_1 (Y+1 vs Y−1). If leakage follows the post-event share of the year, the ratio d_0/d_1 should rise with f (inset). (b) The audit pipeline within each event. (c) The training-year × prediction-year grid. The within-event audit uses the event's own landslides as labels. The forward tests use earlier landslides as labels and a new event for testing; their scenarios F1–F4 occupy the same four cells.

2. Data and methods

2.1. Events and inventories

The audit covers 18 events with a known trigger date and a public inventory (Table 1): seven earthquakes and eleven rainfall events between 2018 and 2024. For an event on day of year d, the post-event fraction of the calendar year is $f = (365 - d)/365$. It ranges from 0.02 for the Mesetas earthquake of 24 December 2019 to 0.86 for the São Paulo coast rainfall of 19 February 2023.

Five events have manually mapped polygons: Emilia-Romagna (Pizziolo et al., 2024), Jishishan (Jin and Chen, 2025), Eastern Iburi (Zhang et al., 2019), Luding (Liu et al., 2025) and Typhoon Mangkhut in Itogon (Abancó and Jones, 2023; Abancó et al., 2021). Manually labelled rasters from GDCLD (Fang et al., 2024) cover the earthquakes of Mesetas, Palu, Lushan and Pasaman. Eight rainfall events have satellite-mapped points from NASA's Cooperative Open Online Landslide Repository (COOLR; Juang et al., 2019), obtained through the Unified Global Landslide Catalogue (Mancino et al., 2025). Seven of them are the seven largest COOLR events of 2022–2023 by point count, selected on size before any result was available. Hurricane Helene is represented by rapid-response points (Burgi et al., 2025).

The initial event list was frozen before any embedding was extracted. Two out-of-sample rounds followed, each with a prediction frozen before the data of its events were read (Sect. 2.10; time stamps in Supplementary Table S3). The first added Iburi, Luding and Typhoon Nalgae to fill the range $0.15 < f < 0.35$, and the second added two autumn rainfall events, Helene and Mangkhut. Two events whose labels came from a segmentation model (Hualien 2024 and northern Guangdong 2024) were analyzed as secondary events and are excluded from all pooled results.

Sampling used a 10 m grid in each event's UTM zone. Each landslide object (a polygon or a connected component of a raster label) contributed one point at its highest pixel in the Copernicus GLO-30 DEM (ESA, 2022), which approximates the crown, and point inventories contributed their points after de-duplication on a 30 m grid. Events with a mapped area received two controls per landslide, drawn at random inside that area (the label footprint for GDCLD and otherwise the convex hull plus 1 km), 100–2,000 m from the nearest landslide pixel and on slopes steeper than 5°. Because the COOLR events have no mapped area, their candidate controls were random offsets of 300–3,000 m from the positives, three per landslide (six for Nalgae), and candidates within 200 m of any positive or on slopes of 5° or less were discarded. For Nalgae, two of the remaining candidates per landslide were kept; for the seven other COOLR events all remaining candidates were kept, which gives 0.94–2.05 controls per landslide (Table 1). For Emilia-Romagna we sampled 15,000 landslides and 30,000 controls at random. In total, the audit uses 61,402 landslide points and 117,059 controls.

Table 1. Events of the audit, ordered by the post-event fraction of the calendar year (f). "Years" gives the annual products used; AlphaEarth starts in 2017, and the year after next (Y+2) was used for 17 events.

Event	Trigger	Date	f	Inventory (source)	Landslides / controls	Years
Mesetas (Colombia)	earthquake	2019-12-24	0.02	manual raster labels (GDCLD; Fang et al., 2024)	1,990 / 3,980	2017–2021
Jishishan (China)	earthquake	2023-12-18	0.04	manual polygons (Jin and Chen, 2025)	10,740 / 21,480	2021–2025
Nalgae, Mindanao (Philippines)	rainfall	2022-10-28	0.18	satellite-mapped points (COOLR)	208 / 416	2020–2024
Helene, southern Appalachians (USA)	rainfall	2024-09-27	0.26	rapid-response points (Burgi et al., 2025)	2,213 / 4,426	2022–2025
Palu (Indonesia)	earthquake	2018-09-28	0.26	manual raster labels (GDCLD)	1,522 / 3,044	2017–2020
Mangkhut, Itogon (Philippines)	rainfall	2018-09-15	0.29	manual polygons (Abancó and Jones, 2023)	1,100 / 2,200	2017–2020
Eastern Iburi (Japan)	earthquake	2018-09-06	0.32	manual polygons (Zhang et al., 2019)	5,625 / 11,250	2017–2020
Luding (China)	earthquake	2022-09-05	0.32	manual polygons (Liu et al., 2025)	8,385 / 16,770	2020–2024
Chittagong (Bangladesh)	rainfall	2023-08-16	0.38	satellite-mapped points (COOLR)	1,764 / 2,921	2021–2025
Northern Vietnam	rainfall	2023-08-04	0.41	satellite-mapped points (COOLR)	1,891 / 3,053	2021–2025
Fujian (China)	rainfall	2023-07-28	0.43	satellite-mapped points (COOLR)	345 / 691	2021–2025
Luzon (Philippines)	rainfall	2023-07-26	0.43	satellite-mapped points (COOLR)	3,133 / 6,422	2021–2025
Lushan (China)	earthquake	2022-06-01	0.58	manual raster labels (GDCLD)	1,286 / 2,572	2020–2024
Agatha (Mexico)	rainfall	2022-05-30	0.59	satellite-mapped points (COOLR)	3,756 / 3,527	2020–2024
Emilia-Romagna (Italy)	rainfall	2023-05-16	0.63	manual polygons (Pizziolo et al., 2024)	15,000 / 30,000	2021–2025
Freddy (Malawi)	rainfall	2023-03-12	0.81	satellite-mapped points (COOLR)	1,634 / 2,948	2021–2025
Pasaman, West Sumatra (Indonesia)	earthquake	2022-02-25	0.85	manual raster labels (GDCLD)	484 / 968	2020–2024
São Paulo coast (Brazil)	rainfall	2023-02-19	0.86	satellite-mapped points (COOLR)	326 / 391	2021–2025

COOLR: Juang et al. (2019), via Mancino et al. (2025). Emilia-Romagna: random subsample of the regional inventory.

2.2. Annual representations

We used the annual Satellite Embedding V1 product of AlphaEarth Foundations (Brown et al., 2025) for 2017–2025, read from the public Source Cooperative mirror of the Earth Engine collection (`tge-labs/aef/v1/annual`). The product stores 64-dimensional unit vectors at 10 m as 8-bit integers v, which we de-quantized as $(v/127.5)^2 \cdot \mathrm{sign}(v)$. Blocks were downloaded with byte-range requests and checked for completeness, decodability, unit norm and consistent masks across bands before use. The 4,049 blocks read in this study, including the 457 blocks of the year after

next, came from 291 source files, last modified between November 2025 and March 2026 (Supplementary Table S18).

The precomputed annual TESSERA representations (Feng et al., 2025) are 128-dimensional 8-bit vectors with a per-pixel scale factor, which we read pixel by pixel from the Source Cooperative archive. Each event used one version: v1 for Emilia-Romagna, Fujian, Helene, Jishishan, Luding, Lushan and Mesetas, and v1.1-cam for Agatha, Freddy and São Paulo, where v1 coverage was insufficient.

Plain Sentinel-2 composites were built from Level-2A scenes of the Earth Search catalogue for the same calendar years. For each MGRS tile and month we took the least cloudy scene with less than 60% cloud cover, so a year contributes at most 12 scenes, and scene classes 4–7 counted as clear. Each composite has nine channels: per-pixel medians of blue, red, near-infrared and SWIR1 reflectance and of NDVI, NDMI and a bare-soil index, plus the 10th and 90th percentiles of NDVI. The same scenes were also composited over the 12 months before and the 12 months after each event day.

Slope, the sine and cosine of aspect, Laplacian curvature, local relief in a 330 m window and elevation were derived from the Copernicus GLO-30 DEM. Land cover came from ESA WorldCover 2021 (Zanaga et al., 2022). The forward tests also used upslope area and mean annual precipitation where available (Sect. 2.8).

2.3. Models

The point model is LightGBM (Ke et al., 2017) applied to the vector of the 10 m pixel at each point, with fixed settings: 400 trees, a learning rate of 0.05, 63 leaves, and row and feature subsampling of 0.8. The patch model, also used without tuning, is the two-dimensional CNN of Cheng et al. (2026), with two convolution and max-pooling stages ($C \to 2C \to 4C$ channels) and three fully connected layers ($16C \to 8C \to 2C \to 2$) with a dropout rate of 0.3. Its input is a patch of 11×11 cells of 30 m, each the mean of 3×3 de-quantized 10 m pixels, with $C = 64$ for AlphaEarth and $C = 9$ for Sentinel-2. We trained it with Adam (learning rate 10^{-3}, batch size 512), a cross-entropy loss and polynomial learning-rate decay for at most 200 epochs, with early stopping on a 15% validation split (patience 10), and averaged its predictions over three seeds.

2.4. Paired year-swap audit

Within each event, points were assigned to spatial folds by k-means clustering of their coordinates (five folds, or ten for Emilia-Romagna), and training points within 500 m of any test point were removed. For each input year we computed out-of-fold predictions and their AUC, from which three paired contrasts follow: the event-year increment d_0 = AUC(Y) − AUC(Y−1); the placebo, AUC(Y−1) − AUC(Y−2), which measures drift between two pre-event years; and the year-after increment d_1 = AUC(Y+1) − AUC(Y−1). Points, controls, folds and model settings are identical across years, so each contrast isolates the input year. Palu, Iburi and Mangkhut have no placebo, because AlphaEarth starts in 2017.

Uncertainty came from a spatial-cluster bootstrap in which points were grouped into 30 k-means clusters (100 for Emilia-Romagna) and the clusters were resampled 1,000 times. Because the same resamples were used for every year, all differences are paired.

Events were pooled by DerSimonian–Laird random-effects meta-analysis (DerSimonian and Laird, 1986). Because between-event heterogeneity is large, we repeated all pooling with the REML estimator of the between-event variance (Viechtbauer, 2005) and Hartung–Knapp–Sidik–Jonkman (HKSJ) intervals (Hartung and Knapp, 2001; IntHout et al., 2014). We also pooled the placebo-corrected increment d_0 − placebo, a difference in differences that asks whether the event-year increment exceeds ordinary drift between years.

The placebo was tested for equivalence to zero with two one-sided tests (TOST; Schuirmann, 1987; Lakens, 2017). The margins were fixed before the main analyses at about one tenth of the effects seen in pilot runs: ±0.01 AUC, against pilot event-year increments of 0.09–0.13, and ±0.02 for map capture, so that drift below these margins cannot change any conclusion. Because any fixed margin is a choice, we also report the smallest margin at which equivalence would be concluded (Supplementary Table S17). As a proxy for map use, we report the share of landslides scoring above the 90th percentile of the control scores.

2.5. Training-year × prediction-year decomposition

An event-year audit changes the inputs of the training points and of the test points at the same time. To separate the two, we refitted every fold model with the inputs of year a and applied it to the test fold with the inputs of year b, for $a, b \in \{\mathrm{Y}-1, \mathrm{Y}\}$ (Fig. 1c). We write $\mathrm{AUC}(a \to b)$ for the resulting out-of-fold AUC. The prediction-time component, $\mathrm{P} = \mathrm{AUC}(\mathrm{Y}-1 \to \mathrm{Y}) - \mathrm{AUC}(\mathrm{Y}-1 \to \mathrm{Y}-1)$, is the effect of event-year inputs at prediction for a cleanly trained model. The training component, $\mathrm{T} = \mathrm{AUC}(\mathrm{Y} \to \mathrm{Y}-1) - \mathrm{AUC}(\mathrm{Y}-1 \to \mathrm{Y}-1)$, is the effect of event-year training on pre-event inputs. The interaction, $\mathrm{I} = d_0 - \mathrm{P} - \mathrm{T}$, is the remainder, so the three components add up to d_0 within each event. The diagonal cells reproduce the audit exactly. Uncertainty and pooling follow Sect. 2.4, and the interpretation rules were prespecified.

2.6. Dose–response and recovery of the year-after reference

If leakage comes from the post-event part of the calendar year, the ratio $r = d_0/d_1$ should rise with f. Because the raw ratio is unstable when d_1 is small, and d_0 and d_1 are correlated through their shared baseline, we fitted a joint errors-in-variables random-effects model (Supplementary Text S1). For event i, (d_{0i}, d_{1i}) is bivariate normal with mean $(r_i \mu_i, \mu_i)$ and the bootstrap covariance. The event's post-event signal μ_i is integrated out by Gauss–Hermite quadrature. The ratio follows $r_i = A \cdot g(f_i) + \eta_i$, where g is a logistic function with half-saturation point f_{50} and A is the plateau. Events without a visible post-event signal ($\mu_i \approx 0$) carry little information, so no rule for excluding them is needed. We tested for a dose–response with a one-sided likelihood-ratio test of the slope b in a linear version, $r_i = a + b \cdot f_i + \eta_i$.

We report f_{50} with its profile-likelihood interval, evaluated between 0.02 and 0.80. Ratios of single events quoted in the text are ratios of the full-sample increments, as used by the joint model.

The year-after product covers lags of f to $f + 1$ years after the event. If scars recover, d_1 falls as f rises, and the ratio can rise for that reason alone. To address this coupling, we first extracted the products of the year after next (Y+2) for 17 events. From the events with a visible year-after signal, we estimated the share of the post-event signal retained over one further year as $q = \Sigma d_2/\Sigma d_1$, with d_2 = AUC(Y+2) − AUC(Y−1). We then refitted the dose–response with d_1 rescaled to a common lag, $d_1 \cdot \exp(\lambda f)$, where $\lambda = -\ln q$. Second, because the Sentinel-2 composites can be cut at any date, we replaced their d_1 with the increment of a composite of the 12 months after the event day, a reference with the same lag for every event. This check used the patch model and a LightGBM model on the nine channels of the central 30 m cell of each patch, with the folds and bootstrap clusters of the composite comparison (Sect. 2.8).

2.7. Map-level evaluation

For Emilia-Romagna and the eight other events with complete manual inventories, we produced out-of-fold susceptibility maps on 30 m grids, with AlphaEarth vectors de-quantized at 10 m and averaged to 30 m. The map domain was the mapped area on slopes steeper than 5°, within 2 km of a mapped landslide (the sampling frame of the controls) and with valid embeddings in all years. Landslide area consisted of the cells whose centre falls inside a landslide polygon, or which contain any landslide pixel of a GDCLD raster. Each cell was predicted by the model of its own fold region, which was trained only on points more than 500 m from that region. We report the share of landslide area within the top 5%, 10% and 20% of the domain area ("capture") and the AUC of landslide cells against all domain cells. Intervals came from a spatial-cluster bootstrap after assigning each cell to its nearest cluster.

2.8. Other annual representations and forward tests

The audit was repeated with the point model on TESSERA vectors for ten events with sufficient coverage. AlphaEarth was recomputed on exactly the same points, folds and resamples. Both model families were also trained on Sentinel-2 composites and on AlphaEarth for 15 events. These events used spatial point subsets fixed before the analysis, with the same folds for both inputs. The composites used only scenes in each point's own UTM zone. Points without any own-zone scene used the neighbouring zone in all years, a rule amended before any affected result was seen. To compare the year-to-year consistency of the two embedding products, we computed a stability index at control points, $(c_{\text{same}} - c_{\text{rand}})/(1 - c_{\text{rand}})$. Here c_{same} is the median cosine similarity of a site's vectors in two consecutive pre-event years, and c_{rand} is that of random pairs of sites.

The forward tests train on landslides mapped before an event and predict that event in three regions (Table 3). In Lushan, the training labels are the landslides

of the April 2013 earthquake (Xu et al., 2015), nine years before the June 2022 test event. Labels inside the hull of the 2022 test points plus 1 km were removed, which left 8,833 landslides and 17,666 controls drawn by the rules of Sect. 2.1. The test set comprised the 1,286 landslides and 2,572 controls of the audit. In western North Carolina, the training labels are 8,188 records of the North Carolina Geological Survey in the USGS landslide inventory (Belair et al., 2019). We used records with a confidence of at least 5 that are dated before 2024 or undated. They are mostly debris flows and debris slides. The test set comprised 2,025 landslides of Hurricane Helene (September 2024) and 3,685 controls within the training extent. In Emilia-Romagna, the training labels are 30,000 crowns from the Italian landslide inventory IFFI (Trigila et al., 2010), mostly complex landslides (63%) and soil creep (27%). IFFI polygons overlapping a 2023 landslide with IoU > 0.5 were removed, and training controls lay more than 100 m from any IFFI polygon. The test set comprised 20,000 crowns and 40,000 controls of the May 2023 event. IFFI records carry no event dates, and the compiled snapshot is dated April 2024, after the event, which makes the Emilia-Romagna test a historical-inventory forward test whose temporal independence rests on the exclusions described below.

The static factors were the terrain factors, land cover and log upslope area, computed with pysheds (Bartos et al., 2024), in all three regions. Emilia-Romagna and North Carolina also used a precipitation climatology (E-OBS 1991–2020, Cornes et al., 2018; PRISM normals, Daly et al., 2008).

Six scenarios combine these inputs, starting from a baseline L that uses the static factors only. In the legitimate scenario F1, training and prediction both use the embeddings of the year before the event (Y−1). F2 trains on Y−1 but predicts with the event-year (Y) embeddings, F3 uses Y for both, and F4 trains on Y and predicts with Y−1. A sixth scenario, L + F1, combines the static factors with the Y−1 embeddings. All forward models were untuned LightGBM with 500 trees and 63 leaves. Paired differences were bootstrapped over spatial clusters of the test points.

To check the temporal independence of the forward results, we retrained the North Carolina models on dated records only and, separately, after removing training landslides within 100 m of any Helene point. In Emilia-Romagna, we removed training crowns within 100 m or 250 m of any 2023 landslide. For spatial independence, we kept only test landslides and controls more than 50, 100, 250 or 500 m from the earlier inventory (100, 250 or 500 m in Lushan). To test whether earlier landslides already resemble fresh scars, we defined a "scar direction" in embedding space as the mean change of the test embeddings between Y−1 and Y at the test landslides, minus that at the test controls. We projected the Y−1 embeddings of the training points onto this direction and measured how well the projection separated training landslides from training controls (projection AUC).

2.9. Follow-up analyses of an outlier

Typhoon Mangkhut leaked more than the dose–response predicted (Sect. 3.8), and we tested four prespecified explanations. The first was that the dose is better

measured by the share of clear Sentinel-2 observations after the event than by calendar time. The second was that part of the inventory predates the typhoon, which we assessed by phenology-corrected NDVI dating of the inventory polygons after checking the method on the instantaneous Iburi earthquake. The third was faster recovery in tropical events, assessed from NDVI at the landslides, and the fourth was disturbance by nearby mining, assessed by excluding points within 500 m or 1 km of mapped mining areas (Maus et al., 2022; OpenStreetMap).

2.10. Prespecification, software and reporting

Before each analysis, its design and decision criteria were written into a time-stamped analysis log; Supplementary Table S10 lists all criteria and outcomes. Two out-of-sample predictions were also frozen, with SHA-256 hashes of their text and code, before their data were extracted. Because the log and the hashes were kept locally and were not deposited with a registry or other third party, we use the term prespecified for these analyses. The first prediction stated that at least two of three transition-zone events would show $d_0/d_1 < 0.8$. The second stated that, for two autumn rainfall events (Helene and Mangkhut), both ratios would fall below 0.9, the rainfall-only slope would be significant and f_{50} would fall within the earlier interval. All computations ran in a Docker container (Python 3.10, LightGBM 4.7.0, scikit-learn 1.7.2, PyTorch 2.11) on NVIDIA RTX 2080 Ti GPUs. Supplementary Text S4 maps every number, table and figure to the code that produced it.

3. Results

3.1. Within-event audit

AlphaEarth embeddings carried substantial pre-event skill: with the prior-year product, the median out-of-fold AUC across the 18 events was 0.81 for the point model and 0.80 for the patch model. Replacing that product with the event-year product inflated the AUC in all 18 events for the point model, by 0.087 on average (95% CI 0.065–0.110), and in 16 of 18 events for the patch model, by 0.071 (0.048–0.093) (Fig. 2; Table 2).

The swap between two pre-event years was equivalent to zero for both models: +0.002 (−0.003 to 0.007) and −0.002 (−0.006 to 0.003), with TOST $p = 0.001$ and < 0.001. Both placebos would be equivalent to zero for any margin of 0.008 AUC or more under either pooling method (Supplementary Table S17), less than a tenth of the event-year increment. Subtracting each event's own placebo left placebo-corrected increments of 0.085 (0.057–0.113) and 0.064 (0.035–0.093), positive in 14 of 15 events for both models, so ordinary drift between years accounts for very little of the inflation. REML pooling with HKSJ intervals gave event-year increments of 0.088 (0.062–0.114) and 0.071 (0.043–0.098), and placebo equivalence still held ($p = 0.011$ and 0.002).

The year-after product raised the AUC by 0.104 and 0.078. With the event-year product, the share of landslides scoring above the 90th percentile of the control scores rose on average from 0.47 to 0.70 for the point model and from 0.48 to 0.67

for the patch model. The patch model's increment was 0.015 (0.005–0.026) smaller than the point model's, a modest reduction that may come from its coarser 30 m cells or from its spatial context.

At Mesetas (f = 0.02), an earthquake on 24 December, almost no post-event observation enters the event-year product, and at Jishishan (f = 0.04) the landslides are also tiny, with a median area of 233 m². Together with Nalgae, whose satellite-mapped points showed no visible post-event signal even in the following year, these were the three events with small or absent increments.

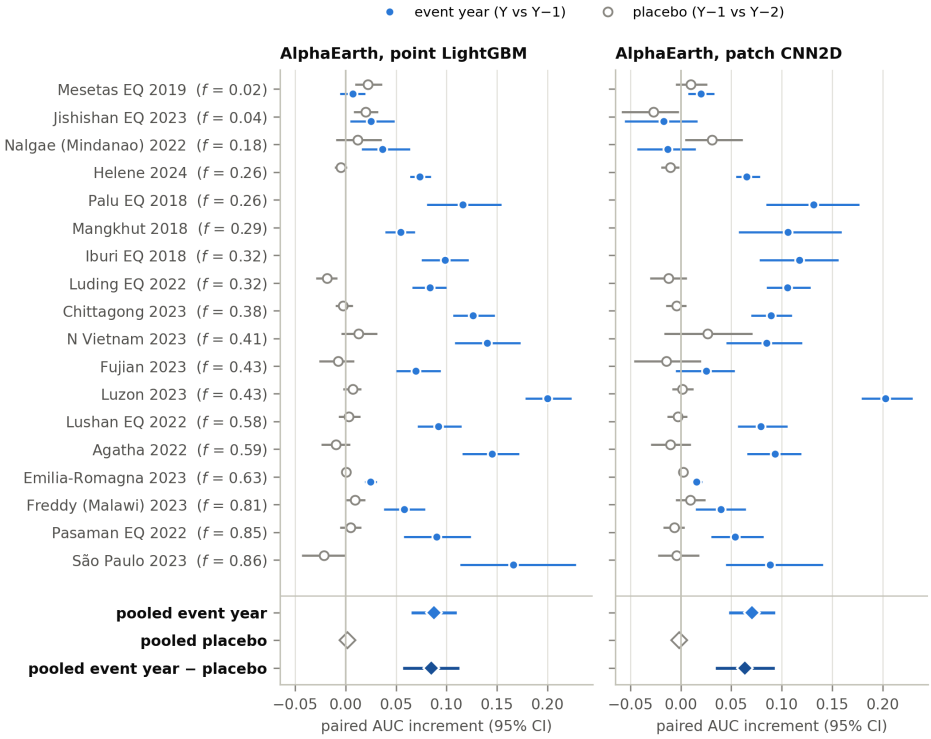


Fig. 2. Event-year and placebo increments for the 18 events (AlphaEarth), for the point model on the 10 m vector (left) and the patch model on 11 × 11 cells of 30 m (right). Bars are spatial-cluster bootstrap 95% CIs. Diamonds show the DerSimonian–Laird pooled event-year increment, placebo and placebo-corrected increment. Events are ordered by f.

Table 2. Pooled audit results by representation and model (random-effects means and 95% CIs, AUC units).

Representation	Model	Points	k	Event year d_0	Placebo (TOST p)	d_0 − placebo	Year after d_1	Dose–response slope p	f_{50} (95% CI)
AlphaEarth	point LightGBM	audit	18	+0.087 (0.065, 0.110)	+0.002; 0.001	+0.085 (0.057, 0.113)	+0.104 (0.076, 0.133)	0.0005	0.24 (0.06, 0.53)
AlphaEarth	patch CNN2D	audit	18	+0.071 (0.048, 0.093)	−0.002; < 0.001	+0.064 (0.035, 0.093)	+0.078 (0.052, 0.104)	0.0003	0.26 (0.12, 0.32)[a]
TESSERA	point LightGBM	TESSERA subset	10	+0.104 (0.073, 0.135)	+0.003; 0.15	+0.103 (0.058, 0.147)	+0.121 (0.089, 0.154)	0.00002	0.33 (0.16, ≥ 0.80)
AlphaEarth	point LightGBM	TESSERA subset	10	+0.071 (0.047, 0.094)	−0.002; 0.030	+0.072 (0.044, 0.101)	+0.088 (0.055, 0.121)	0.0003	0.31 (0.24, 0.38)
Sentinel-2 composite	patch CNN2D	composite subset	15	+0.126 (0.076, 0.175)	−0.015; 0.68	+0.139 (0.075, 0.202)	+0.179 (0.100, 0.258)	0.004	0.32 (≤ 0.02, ≥ 0.80)[a]
Sentinel-2 composite	point LightGBM	composite subset	15	+0.137 (0.066, 0.207)	−0.014; 0.63	+0.159 (0.074, 0.245)	+0.188 (0.125, 0.252)	0.046	0.33 (≤ 0.02, ≥ 0.80)[a]
AlphaEarth	patch CNN2D	composite subset	15	+0.073 (0.042, 0.103)	−0.009; 0.47	+0.072 (0.029, 0.114)	+0.083 (0.049, 0.116)	0.0001	0.39 (0.18, ≥ 0.80)
AlphaEarth	point LightGBM	composite subset	15	+0.098 (0.060, 0.137)	−0.005; 0.25	+0.093 (0.049, 0.137)	+0.126 (0.083, 0.169)	0.0002	0.32 (0.28, 0.35)[a]

Placebo and placebo-corrected values use the events with a Y−2 product (15, 10 and 13 events for the three point sets). [a] Step-like fit: the logistic scale reached its lower bound and f_{50} marks the location of the step. Bounds written as ≤ 0.02 or ≥ 0.80 reach the edge of the evaluated range.

3.2. Training-year and prediction-year components

For a model trained on pre-event inputs, switching only the test inputs to the event year moved single events in both directions (Fig. 3). The change ranged from −0.068 (Iburi) to +0.052 (Pasaman) for the point model and from −0.104 (Iburi) to +0.072 (Mangkhut) for the patch model. Its 95% interval lay above zero in 6 and 4 events and below zero in 4 and 5 events. Pooled over events, the change was +0.0006 (−0.011 to 0.013) and −0.011 (−0.027 to 0.006), and the upper bounds exclude a systematic inflation larger than 0.013 and 0.006 AUC (0.015 and 0.011 with HKSJ intervals), less than a fifth of the event-year increment. Used only at prediction, event-year inputs thus moved single events up or down and left the pooled score essentially unchanged. A plausible reason for the two signs is that fresh scars resemble different things in the pre-event feature space: steep unstable slopes in some events, bare or cultivated ground in others.

A model trained on event-year inputs and applied to pre-event inputs lost 0.043 (0.031–0.055) and 0.053 (0.034–0.072) of AUC, in 18 and 16 of the 18 events. The interaction of the two, positive in all 18 events for both models, amounted to +0.135 and +0.133; it exceeds the event-year increment because it also offsets the loss of the training-only case. Within each event d_0 = P + T + I, whereas each component is pooled separately across events, so the pooled values need not add up exactly.

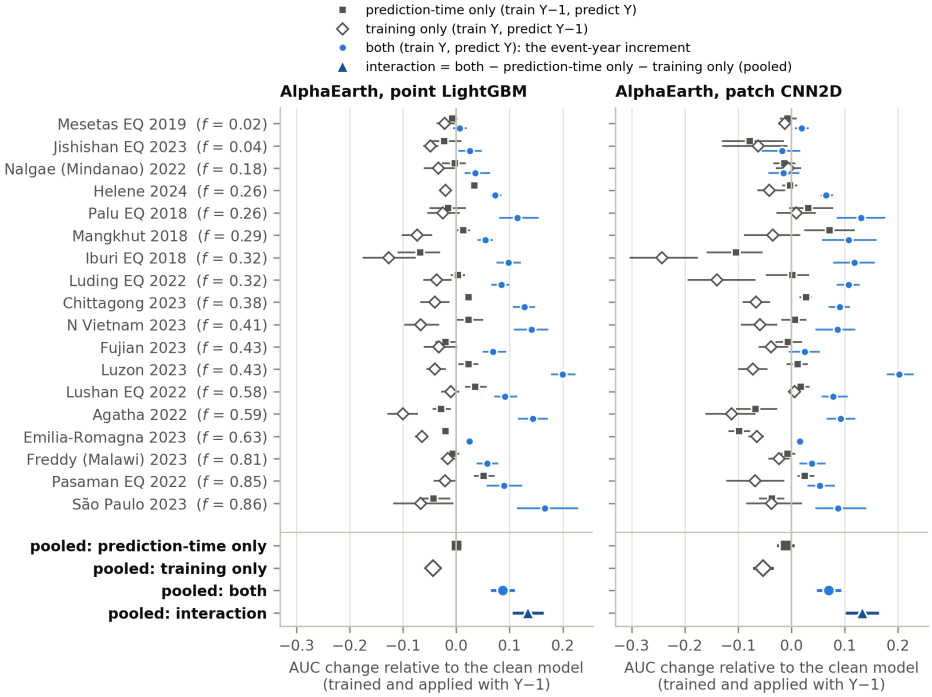
Taken together, the three components show that the event-year audit rewards a model for recognizing what the event did to the landscape. In the event-year inputs, the training landslides carry their own fresh scars, which the model learns and finds again at the test landslides. When either the training or the test inputs lack this signature, the gain disappears; with pre-event test inputs, the model trained on the event year even loses skill, because the features it relies on do not yet exist.

3.3. Dependence on the post-event fraction of the year

The ratio d_0/d_1 rose with f (Fig. 4; Table 2). In the joint model fitted to the 18 events, the slope was +0.95 for the point model (one-sided p = 0.0005) and +1.35 for the patch model (p = 0.0003). The half-saturation point f_{50} was 0.24 (0.06–0.53) and 0.26 (0.12–0.32), corresponding to events in late September or early October, and the patch-model transition was step-like. All ten events with $f \geq 0.37$, that is, events before mid-August, had ratios of at least 0.90 in both models, although the scatter around the curve was large (τ = 0.14 and 0.23 in ratio units).

The relation held among the seven earthquakes alone, which span f from 0.02 to 0.85 ($p < 0.0001$). Among the rainfall events alone it held for the point model (p = 0.040) but not for the patch model (p = 0.16). Trigger type and inventory quality are confounded in this comparison: eight of the eleven rainfall events have satellite-mapped point inventories, whereas every earthquake has a polygon or raster inventory.

Between the year after and the year after next, the post-event signal retained 77% of its size for the point model (event bootstrap 66–85%) and 76% for the patch model (59–90%), so the year-after reference does decay, at an annual rate of λ



Same points, folds and bootstrap clusters as Fig. 2; 95% CIs from 1,000 spatial-cluster resamples; pooled rows: DerSimonian–Laird random effects. The interaction was positive in all 18 events for both models. Each pooled row is pooled separately, so the pooled terms need not add up exactly.

Fig. 3. Training-year × prediction-year decomposition within each event (AlphaEarth; same points, folds and bootstrap clusters as Fig. 2). Markers give the AUC change relative to the clean model, which is trained and applied with Y−1. Squares show event-year inputs at prediction only, open diamonds in training only, and circles in both, which is the event-year increment. The bottom rows are random-effects means, including the pooled interaction (triangles). Within each event the increment equals the sum of the three components; the pooled rows are pooled separately and need not add up exactly.

= 0.26–0.27. Rescaling d_1 to a common lag did not remove the dose–response: the slope remained significant (p = 0.004 and 0.002; $p \leq 0.013$ at either end of the interval of λ), and f_{50} barely moved (0.23 and 0.26). What changed was the plateau, which fell from 1.16 and 1.14 to 0.96 and 0.99. The recovery of the reference had lifted it above one, which is why event-year signals often exceeded year-after signals at high f.

Because they can be cut at the event date, the Sentinel-2 composites allow an independent check (Fig. 4, right; Supplementary Table S13). For the LightGBM model on the central 30 m cell, the calendar year-after reference gave a slope p of 0.004, f_{50} = 0.33 and τ = 0.70. With a reference built from the 12 months after the event day, which has the same lag for every event, the dose–response remained and the scatter fell to τ = 0.23 (p = 0.0006, f_{50} = 0.34, plateau 0.96). For the patch model, the slope also remained significant with the fixed reference (p = 0.011, against 0.004 with the calendar reference), and τ fell from 0.65 to 0.24, although its logistic fit no longer located f_{50} because the scale reached its upper bound. With the LightGBM model, the calendar year-after increment declined with f (Spearman −0.30), as the recovery coupling predicts, whereas the fixed-window increment did not (+0.01); with the patch model both declined slightly (−0.25 and −0.23).

Across representations and references, the point estimates of f_{50} fell between 0.23 and 0.39: an annual product carries half of the full post-event signal once about a quarter to a third of the year has passed after the event. We read this range as an empirical transition estimate for the products and events studied here, because the intervals were wide for TESSERA and the composites and several fits were step-like (Table 2). The first prespecified out-of-sample prediction, for the transition-zone events, was met: with the point model, Iburi (0.65) and Luding (0.61) fell below 0.8. When the prediction was first evaluated, on an earlier point sample, the ratios were 0.64 and 0.60 (Supplementary Table S10).

3.4. Other annual representations

TESSERA leaked more than AlphaEarth on the same points (Table 2; Supplementary Table S2). Over the six events with $f \geq 0.35$ and a visible post-event signal, as the prespecified criterion required, its event-year increment was +0.134 (0.090–0.179). Over all ten events it was +0.104, against +0.071 for AlphaEarth on the same points, a difference of 0.029 (0.013–0.044), with TESSERA larger in nine of ten events. Its placebo-corrected increment was +0.103 (0.058–0.147), and its dose–response was strong (slope p = 0.00002; Spearman correlation between f and the ratio 0.92; f_{50} = 0.33).

The TESSERA placebo, however, was not equivalent to zero within ±0.01 (p = 0.15). It would be equivalent within ±0.02 (smallest margins 0.014 and 0.017; Supplementary Table S17), and single-event placebos ranged from −0.037 to +0.041, a noise level consistent with the lower cross-year stability of TESSERA. At control points, consecutive-year TESSERA vectors had cosine similarities of 0.84–0.91, against 0.95–0.98 for AlphaEarth, which gives stability indices of 0.44–0.81 against 0.80–0.96. The TESSERA similarities hardly varied between years (0.914, 0.908

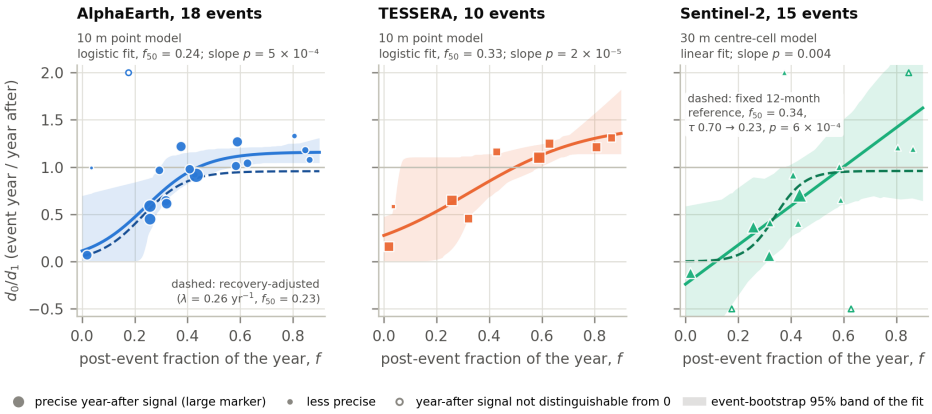


Fig. 4. Dose–response in three annual representations: the ratio of the event-year to the year-after increment against f. AlphaEarth and TESSERA use the 10 m point model. The Sentinel-2 panel uses LightGBM on the central 30 m cell of the composite patches, for which a fixed 12-month reference exists; the 10 m point model of Table 2 gives a weaker calendar-reference slope (p = 0.046). Marker area scales with the precision of the year-after signal. Small open markers are events whose year-after increment is indistinguishable from zero, so their ratios carry little information. Ratios beyond −0.5 or 2 are drawn at the axis limits. Solid lines are joint random-effects fits (logistic, or linear where the logistic fit degenerated to a step), and shaded bands are 95% event-bootstrap ranges of these fits. Dashed lines are fits with references free of the recovery coupling: year-after increments rescaled for the recovery measured from the year after next (AlphaEarth), and the fixed 12-month post-event reference (Sentinel-2).

and 0.911 at the Helene controls for 2022→2023, 2023→2024 and 2024→2025), which argues against a production break.

Plain annual median composites of Sentinel-2 leaked as well (Table 2), with gains of +0.126 (0.076–0.175; 14 of 15 events) for the patch model and +0.137 (0.066–0.207) for the point model, and placebo-corrected increments of +0.139 and +0.159. AlphaEarth gained +0.073 at patch level on the same points, so by the prespecified rule the composites were "more sensitive" (difference −0.045, −0.085 to −0.005).

This classification, however, does not account for the baseline: the composites carried almost no transferable pre-event information, with a median pre-event AUC of 0.55 at patch level against 0.72 for AlphaEarth, so their gains start from nearly random ranking. In several events the composites even gave cross-validated AUCs below 0.5, because the relation between spectra and landslides reversed between spatial folds; this covariate shift makes plain composites poor susceptibility predictors in their own right. A composite, unlike the published annual products, can be cut at the event date (Supplementary Table S6). Composites built only from event-year scenes acquired before the event differed from the previous year by a median of +0.03 AUC, whereas post-event composites exceeded it by a median of +0.21.

3.5. Map-level effects

On complete maps of nine events, the event-year input added on average 0.221 (point model; 0.148–0.294) and 0.207 (patch model; 0.135–0.278) of the landslide area to the most susceptible tenth of the map, with a positive gain in all nine events (Figs. 5 and 6). The map effect was large even where the AUC effect was small. In Emilia-Romagna, where the point AUC increment was only +0.025 and the placebo was equivalent to zero within ±0.02, the share of 2023 landslide area in the top 10% rose from 0.51 to 0.67 with the point model and from 0.58 to 0.68 with the patch model. In Iburi, capture rose from 0.15 to 0.61 with the patch model (Fig. 5a), and across the seven events with $f \geq 0.26$ the gains were 0.10–0.46 (0.16–0.46 without Emilia-Romagna). Map gains were a median 3.0–3.7 times the point-AUC gains on the same maps, and the map-level ratio of event-year to year-after gains rose with f (Spearman 0.83–0.90).

Even Mesetas and Jishishan, with $f = 0.02$ and 0.04, gained 0.03–0.07, and the map placebo shows how large such changes can be without leakage. The pooled map placebo of the prespecified test (five events) was not equivalent to zero within ±0.02 (TOST $p = 0.17$ and 0.063). Adding Emilia-Romagna gave $p = 0.08$ and 0.02 with DerSimonian–Laird pooling but 0.18 and 0.06 with HKSJ intervals (Supplementary Table S16). Within ±0.05, every map placebo was equivalent to zero ($p \leq 0.009$; Supplementary Table S17), and single-event map placebos ranged from −0.035 to +0.052. Map changes of a few hundredths therefore lie within the noise of the comparison, whereas the gains of 0.10–0.46 in the seven events with $f \geq 0.26$ are two to nine times larger than it.

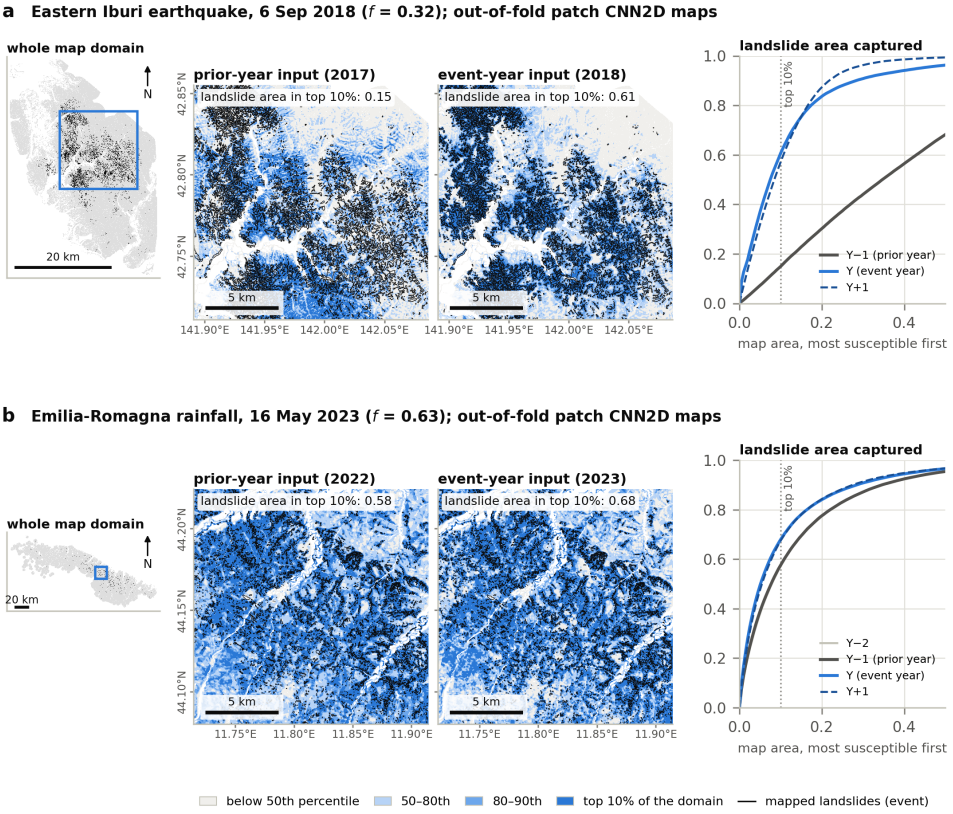


Fig. 5. Example maps of out-of-fold patch-model susceptibility for (a) Eastern Iburi and (b) Emilia-Romagna. The left panels show the whole map domain and the 16 × 16 km window (blue square), chosen automatically as the window with the most landslide area. The middle panels show the maps made with the prior-year and the event-year AlphaEarth product, shaded by the percentile of the score within the whole domain, with the event's landslides outlined. The numbers give the share of landslide area within the top 10% of the domain. The right panels show capture curves for the whole domain; in (b) the Y−2 and Y−1 curves overlap. Scale bars show 20 km (overview) and 5 km (maps).

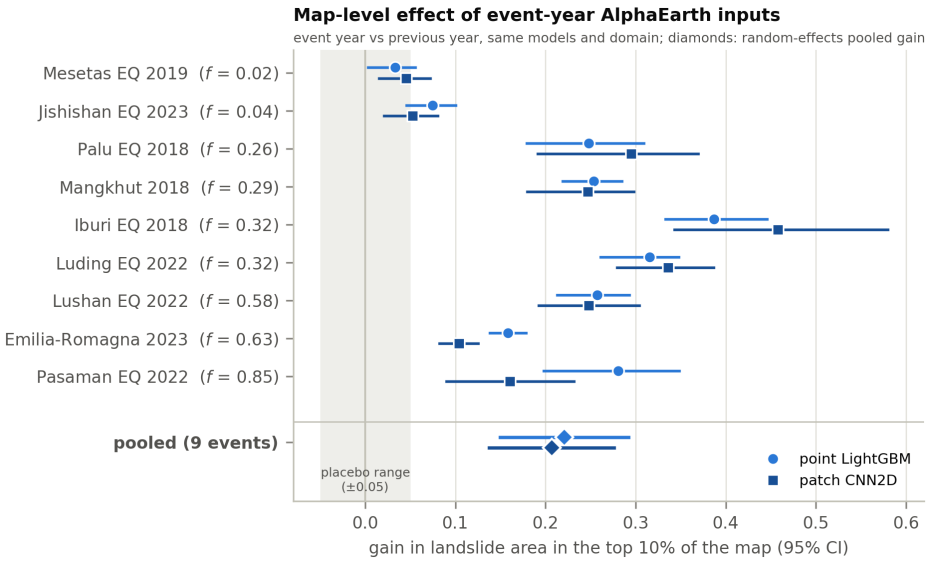


Fig. 6. Map-level effect for nine events with complete inventories: the gain in landslide area within the top 10% of the map when the event-year AlphaEarth product replaces the prior-year product (95% spatial-cluster bootstrap CIs). The shaded band marks the range of the single-event map placebos (about ±0.05). Diamonds are random-effects pooled gains.

3.6. Re-analysis of a published setting

Cheng et al. (2026) found that AlphaEarth embeddings outperform conventional conditioning factors for the May 2023 landslides in Brisighella and Modigliana (Emilia-Romagna), using the 2023 embeddings with a random 70:30 split. We re-implemented their CNN1D, CNN2D and ViT, added LightGBM, used the same inventory (Ferrario, 2023; Ferrario and Livio, 2024) and changed only the embedding year (Supplementary Table S7). Under the published random split, the event-year increment was +0.011 to +0.034, positive in every seed of every configuration, with placebos within ±0.002. Under spatial five-fold cross-validation with a 500 m buffer, it rose to +0.042 to +0.086, because post-event scars help most when a model must extrapolate. The pre-event embeddings still outperformed our six terrain factors under spatial cross-validation (+0.034 to +0.060); since the original study used 14 conditioning factors, this difference is best read as an upper bound on the legitimate advantage of the embeddings. On maps produced as in the original study, the event-year input raised the share of landslide area in the top 10% from 0.375 to 0.454 (CNN2D) and from 0.390 to 0.536 (LightGBM), whereas the terrain factors captured 0.324 and 0.325. The event-year gain thus accounts for 61% (0.079 of 0.130) and 69% (0.146 of 0.211) of the map-level advantage of the published input over the terrain factors. Measured by AUC with the same protocol and sample (Supplementary Table S7), the corresponding shares are 17% for CNN2D (0.011 of 0.064) and 32% for LightGBM (0.027 of 0.085).

3.7. Forward tests in three regions

In all three regions, models trained on earlier landslides scored the new event higher when given event-year inputs at prediction time (F2 − F1; Fig. 7a; Table 3), by +0.024 (0.008–0.039) in Emilia-Romagna, +0.058 (0.043–0.071) in North Carolina and +0.113 (0.092–0.133) in Lushan. In this setting, unlike in the within-event audit, a cleanly trained model responds to the new scars. In the scar-direction analysis (Supplementary Text S6), the pre-event embeddings of the training landslides already stood out from their controls along the direction in which the test landslides, relative to the test controls, moved between the year before and the event year (projection AUCs of 0.645 in North Carolina and 0.595 in Emilia-Romagna). Earlier landslides look partly like fresh scars, so a model that has learned them scores new scars as susceptible.

The prediction-time inflation held under the checks for temporal independence. In North Carolina it was +0.052 with dated pre-2024 records only (3,222 landslides) and +0.058 after removing training landslides near any Helene point, and in Emilia-Romagna it was +0.027 and +0.049 after removing IFFI crowns within 100 m or 250 m of any 2023 landslide. Restricting test sites to more than 50–500 m from the earlier inventory (Fig. 7b) gave increments of +0.061 to +0.073 in North Carolina, +0.029 to +0.037 in Emilia-Romagna and +0.117 to +0.134 in Lushan, and only the Emilia-Romagna interval beyond 500 m (924 test landslides) included zero.

Whether legitimate pre-event embeddings beat terrain factors (F1 − L) depended on where the new failures occurred. In North Carolina the embeddings helped overall (+0.037, 0.019–0.057; +0.041 with dated records only), and the advantage shrank with distance from earlier landslides, to +0.016 (−0.013 to 0.043) beyond 500 m. In Lushan the advantage was +0.069 (0.013–0.114) for the 608 of 1,286 test landslides within 100 m of a 2013 landslide and −0.016 for the others. Overall it was +0.024 (−0.025 to 0.071), so by the prespecified rule this region could not decide the question. The Lushan values beyond 250 m and 500 m (+0.008 and +0.038; Fig. 7b) rest on 326 and 155 test landslides, and their intervals, from −0.076 to 0.096 and from −0.067 to 0.112, are too wide to show a trend. In Emilia-Romagna, whose earlier inventory consists mostly of old complex landslides and soil creep unlike the shallow failures of 2023, the embeddings did worse than terrain factors at every distance (−0.076 to −0.091). Static-factor skill itself fell from an AUC of 0.629 to 0.481 when the IFFI records near the 2023 failures were removed. TESSERA did worse than terrain factors in North Carolina (−0.065), and its model trained on 2023 lost skill on 2024 inputs (−0.028), consistent with its low cross-year stability.

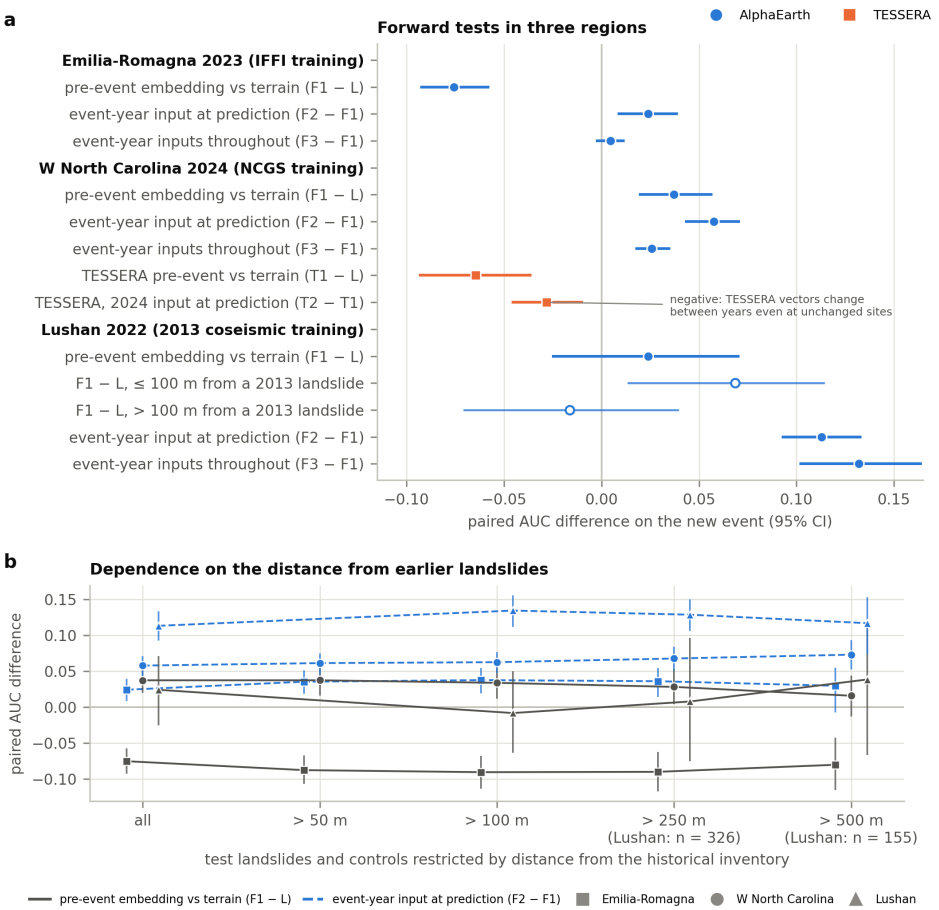


Fig. 7. Forward tests. (a) Paired AUC differences on the new event in three regions (95% cluster-bootstrap CIs). F1 − L compares legitimate pre-event embeddings with static factors, F2 − F1 adds event-year inputs at prediction, and F3 − F1 uses event-year inputs throughout. For Lushan, open circles split F1 − L by whether the test landslide lies within 100 m of a 2013 landslide. Squares show the TESSERA comparisons in North Carolina: pre-event TESSERA against static factors (T1 − L) and 2024 TESSERA inputs at prediction (T2 − T1). (b) The same differences when test landslides and controls are restricted to sites farther from the earlier inventory. Solid lines show F1 − L and dashed lines F2 − F1. The Lushan subsets beyond 250 m and 500 m contain only 326 and 155 test landslides.

Table 3. Forward tests: AUC on the new event and paired differences (95% CI). L: static factors only; F1: embeddings of the year before the event (Y−1) for training and prediction; F2: trained on Y−1, predicted with the event year (Y); F3: Y for both. The Emilia-Romagna test is a historical-inventory forward test (Sect. 2.8).

Region (training labels → test)	L	F1	F2	F3	F1 – L	F2 – F1	F3 – F1
Emilia-Romagna (IFFI → May 2023)	0.629	0.553	0.577	0.558	−0.076 (−0.093, −0.057)	+0.024 (0.008, 0.039)	+0.005 (−0.003, 0.012)
W North Carolina (NCGS → Helene 2024)	0.725	0.762	0.820	0.788	+0.037 (0.019, 0.057)	+0.058 (0.043, 0.071)	+0.026 (0.017, 0.035)
Lushan (2013 coseismic → June 2022)	0.574	0.598	0.711	0.730	+0.024 (−0.025, 0.071)	+0.113 (0.092, 0.133)	+0.132 (0.101, 0.164)

3.8. Typhoon Mangkhut and the failed second prediction

The second prespecified out-of-sample prediction, for two autumn rainfall events, failed. Helene behaved as expected, with ratios of 0.59 for the point model and 0.50 for the patch model. Mangkhut did not: its ratios were 0.97 and 1.52, against 0.57 and 0.77 expected from the earlier fit, and the rainfall-only slope was not significant for the patch model.

None of the four prespecified follow-up analyses fully explained the anomaly. Weighting the dose by clear-sky observations fitted the 17 other events worse than calendar time, and NDVI declines did not recover faster in tropical events. Almost a quarter of the dated Mangkhut landslides (22.8%) had appeared before the typhoon, but accounting for this raised the predicted ratios only to 0.70 and 0.87. Excluding points near mapped mining areas lowered the point-model ratio to 0.85–0.89 but left the patch-model ratio at 1.26–1.48; because the mapped mining area is small (0.63 km²), unmapped small-scale mining cannot be ruled out. Mangkhut remains an unexplained outlier, and it shows how far a single event can depart from a dose–response that describes a tendency across events.

4. Discussion

4.1. Mechanism of the inflation

According to the decomposition, a model that has learned what the event's surface changes look like scores high whenever its inputs contain them. In a within-event audit the training labels are the event's own landslides, so the model can learn this signature only from event-year training inputs, and the inflation needs event-year inputs on both sides. Used only at prediction, event-year inputs shift single events in either direction without moving the pooled score. In forward use, earlier inventories supply training labels that already look partly like scars in the pre-event products, and a cleanly trained model then responds to new scars at prediction time, by 0.02–0.11 AUC in the three regions. In both settings, the score measures how well the model recognizes the event, not how well it anticipated it.

River-bank and field damage from the same storm also became more landslide-like in event-year models (Supplementary Text S6), so part of the signature comes from surface changes other than the landslides themselves. For evaluation the distinction does not matter, because any post-event surface change violates the temporal constraint of a predictive model.

Steger et al. (2020) described a close parallel in topography: susceptibility models are often built on elevation models acquired after the mapped landslides, so that terrain predictors depict the morphometric signature of past failures. In their comparison, models based on post-failure and on approximated pre-failure topography differed most at fine raster resolution and for larger landslides. Annual embeddings carry the spectral and temporal counterpart of that footprint. The slightly smaller inflation of the 30 m patch model than of the 10 m point model (Sect. 3.1) is consistent with the same dependence on resolution, although the two models also differ in architecture. In the terms of Kaufman et al. (2012), event-year inputs introduce information about the target that would not be legitimately available at the time of prediction, and the learn–predict separation they recommend amounts here to using only products whose year ends before the event.

The same mechanism accounts for the larger inflation under spatial cross-validation in the re-analyzed study, where the event-year increment was +0.011 to +0.034 under a random split and +0.042 to +0.086 under spatial cross-validation (Sect. 3.6). Spatial blocking removes the dependence between nearby training and test samples that inflates random cross-validation (Brenning, 2005; Karasiak et al., 2022), but it also forces the model to extrapolate (Roberts et al., 2017). Fresh scars look alike from one area to the next, so they probably keep their value under extrapolation better than predictors whose relation to failure varies between areas. Spatially separated validation remains necessary for susceptibility models, and inputs observed after the event need a separate check, such as the year-swap audit of Box 1.

In practical terms, the event-year increments of 0.07–0.09 AUC exceed the legitimate advantage of pre-event embeddings over six terrain factors in the re-analyzed setting (+0.034 to +0.060; Sect. 3.6), and on maps a gain of 0.21 moves a fifth of the landslide area into the most susceptible tenth. Post-event products are well suited to mapping an event's landslides, which is the aim of change-detection methods built on multi-temporal imagery (Behling et al., 2014; Scheip and Wegmann, 2021), but maps obtained with them should not be presented as susceptibility assessments.

4.2. Calendar time and the dose–response

An annual product summarizes its year, so its post-event content grows with the post-event part of that year, though faster than in proportion. Proportional averaging would give a ratio equal to f. Instead, half of the full post-event signal was reached once a quarter to a third of the year followed the event (f_{50} = 0.23–0.39, an empirical estimate for these products; Sect. 3.3), and events with $f \geq 0.37$ had ratios of at least 0.90. A post-event state observed for a few months thus weighs more in an annual product than its share of the year.

Because the year-after reference loses about a quarter of its signal per year (q = 0.76–0.77), event-year signals often exceeded year-after signals at high f; put on a common lag, the plateau is close to one (0.96–0.99) and the transition stays where it was. The fixed 12-month reference for the Sentinel-2 composites reaches the same conclusion without any assumption about the decay (Fig. 4), with a significant slope and a scatter that fell from τ = 0.70 to 0.23. A decay over several years is consistent with the gradual revegetation of landslide scars: after the 2008 Wenchuan earthquake, for example, MODIS NDVI time series indicated that 83% of the coseismic landslides had become inactive within a decade (Yunus et al., 2020).

Calendar time also explained the dose better than the share of clear optical observations after the event. This is consistent with both embedding products using radar data and modelling time series instead of cloud-free composites (Brown et al., 2025; Feng et al., 2025), and with the weaker detection of late-year fires in annual embeddings (Knezevic et al., 2026).

4.3. Embeddings, composites and cross-year stability

Plain Sentinel-2 composites leaked as much as AlphaEarth, or more, with the same dose–response, which places the source of the leakage in calendar-year aggregation itself. The practical risk is nevertheless greater for embeddings. Composites carried little transferable pre-event information (median pre-event AUC 0.55 at patch level), so their leakage is conspicuous, whereas embeddings had high pre-event skill (median 0.80–0.81 in the audit) that makes the added post-event information easy to miss. The same caution applies to other dated targets mapped with annual products, such as burned areas and flood extents (Knezevic et al., 2026; Thasma et al., 2026; Zhuang et al., 2026), whenever the aggregation window of the product overlaps the period after the event.

The two embedding products also differ in their stability across years, which matters whenever a model is trained on one year and applied to another. At unchanged sites, TESSERA vectors change more between consecutive years than AlphaEarth vectors (stability index 0.44–0.81 against 0.80–0.96), which makes the TESSERA placebo noisy and makes models trained on one year degrade on the next. Users who train on one year and predict with another should first check the cross-year stability of their product at unchanged sites.

4.4. Forward value of pre-event embeddings

The legitimate forward value of pre-event embeddings was concentrated near earlier landslides: in North Carolina it shrank with distance from mapped landslides, and in Lushan it appeared only for failures within 100 m of a 2013 landslide. In Emilia-Romagna, where the earlier inventory is dominated by old complex landslides and soil creep unlike the shallow failures of 2023, the embeddings did worse than terrain factors everywhere. Together with the scar-direction analysis, this suggests that much of what the embeddings add beyond terrain is a record of existing instability, which predicts reactivations and nearby failures better than first-time

failures. Such a record has value of its own, because landslides tend to follow landslides. In a multi-temporal inventory with 17 time slices, earlier landslides raised the susceptibility of the same ground for about ten years (Samia et al., 2017). In the Collazzone area of central Italy, this path dependency had a characteristic spatial scale of 60 m, and adding it considerably improved a conventional susceptibility model (Samia et al., 2020). The Lushan advantage within 100 m of landslides nine years older is consistent with these scales, and pre-event embeddings may capture part of this legacy where no multi-temporal inventory exists.

Fang et al. (2026) found the same ordering in Taiwan's annual inventories, where previous-year AlphaEarth embeddings predicted newly mapped landslides with high skill. Reactivated pixels were predicted best (ROC-AUC 0.978–0.984) and isolated first-time failures least well (0.866–0.938 in 2020–2023 and 0.791 in 2024). In 2020–2023, 63–68% of the newly mapped area lay on pixels mapped in an earlier inventory. Their skill also fell in 2024, a year of strong earthquake and typhoon forcing, which they interpret as a shift in trigger regime. The forward value of annual embeddings depends on the region and on what the training labels represent and needs case-by-case testing, whereas the inflation from event-year inputs appeared in all three of our regions.

4.5. Recommendations

The results translate into a short checklist for studies that use annual satellite products (Box 1).

Box 1. Temporal provenance checklist for annual satellite products in landslide studies

1. **Use only products whose calendar year ends before the event.** For event-based susceptibility modelling or hindcasting, use Y−1 or earlier, however late in the year the event occurred.
2. **Report a year-swap audit:** AUC(Y) − AUC(Y−1) together with the placebo AUC(Y−1) − AUC(Y−2), on identical points, folds and models. A positive placebo-corrected increment indicates leakage.
3. **Evaluate maps by area**, for example by the share of landslide area within the top 5–20% of the map. Point AUC understates the consequences at map level.
4. **Cut your own composites at the event date.**
5. **Check cross-year stability** at unchanged sites before training on one year and predicting with another.
6. **Report where forward skill comes from**, separating test landslides near earlier landslides from first-time failures.
7. **Document the temporal provenance of every predictor:** the observation window, the product release and file versions, the training period of the underlying model and the inventory date.

The checklist matters most where susceptibility maps enter zoning for land-use planning (Fell et al., 2008). A zoning map evaluated with event-year inputs ranks terrain partly by the scars of the event it is tested on, and its inflated skill makes it look more reliable than it is. Validation on a later event, proposed by Guzzetti et al. (2006) and extended to chrono-validation by Lombardo and Tanyas (2020), tests the use for which a zoning map is made, but it does not guard against this leakage by itself: in our three forward regions, models trained on earlier landslides still gained 0.02–0.11 AUC when the event-year product was used at prediction time. When a zoning map is revised after an event, post-event products may legitimately describe the changed terrain for future use, but they cannot be used to validate the revised map on that event's landslides; its skill has to be judged with pre-event inputs or on later landslides.

4.6. Limitations

The 18 events differ in type and inventory quality, and between-event heterogeneity is large. Only three rainfall events have $f < 0.35$, and trigger type is confounded with inventory type. The point inventories (COOLR and Helene) are biased towards roads and settlements (Guzzetti et al., 2012), and the Mangkhut inventory spans more than a year. The placebo was not equivalent to zero within the prespecified margins in several secondary point sets and at map level, so effects of a few hundredths in single events should not be attributed to leakage. The placebo-corrected increments, however, remained positive, with intervals excluding zero, in every pooled analysis.

We had no access to the internals of the embedding models, so the mechanism is inferred from inputs and outputs. The analyses were prespecified in a local time-stamped log, verifiable only through file hashes and time stamps, and the Emilia-Romagna forward test relies on an undated inventory. Finally, the results refer to AlphaEarth Satellite Embedding V1 and TESSERA v1 and v1.1-cam. The models were untuned, the audit's static factors were limited to terrain and land cover, and the forward tests did not use triggering rainfall.

5. Conclusions

The product of an event year already contains the event. Across 18 dated landslide events, replacing the prior-year AlphaEarth product with the event-year product inflated within-event AUC by 0.07–0.09 beyond ordinary drift between years, and on maps it moved, on average, a fifth of the landslide area into the most susceptible tenth. The inflation arises when models learn the event's surface changes, chiefly its landslide scars. It grows with the post-event share of the calendar year, reaching half its full size when a quarter to a third of the year follows the event, and this relation survives corrections for recovery. A second embedding product and plain Sentinel-2 composites leak in the same way. In forward tests in three regions, models trained on earlier landslides gained 0.02–0.11 AUC from event-year inputs at prediction time, whereas the legitimate forward value of pre-event embeddings

was concentrated near earlier landslides. Three practices avoid the problem: use annual products whose year ends before the event, audit the year swap, and judge maps by area. Where maps support land-use zoning, validation on later events needs the same check of predictor dates.

Data and code availability

All input data are public. They comprise the AlphaEarth Foundations Satellite Embedding V1 (Google and Google DeepMind, CC BY 4.0), read from the Source Cooperative mirror `tge-labs/aef/v1/annual` in October 2026; the TESSERA embeddings v1 and v1.1-cam (Source Cooperative `tessera/tessera`); Copernicus Sentinel-2 Level-2A scenes from the Earth Search catalogue; the Copernicus GLO-30 DEM, ESA WorldCover 2021, E-OBS and PRISM; and the inventories listed in Table 1, IFFI, USLI v3, the 2013 Lushan inventory and the global mining polygons. Supplementary Data S1 and S2 list every embedding file used, with its ETag, size and last-modified date (summary in Table S18). The AlphaEarth Foundations Satellite Embedding dataset is produced by Google and Google DeepMind. The analysis code, the time-stamped analysis log, the frozen predictions with their hashes, the result tables, and the derived point sets, designs and out-of-fold predictions needed to recompute every reported statistic are archived at Zenodo (Du et al., 2026; https://doi.org/10.5281/zenodo.23467612). Files derived from the Unified Global Landslide Catalogue (Mancino et al., 2025) are shared under its CC BY-NC 4.0 licence. Supplementary Tables S1–S18 give the per-event and pooled results.

CRediT authorship contribution statement

Yifan Du: Conceptualization, Methodology, Software, Investigation, Formal analysis, Resources, Visualization, Supervision, Project administration, Writing – original draft, Writing – review & editing. **Tianhe Zheng:** Investigation. **Peiyan Yang:** Investigation. **Yibo Li:** Data curation, Resources. **Junhang Zhou:** Validation, Formal analysis, Visualization. **Kun Yang:** Writing – original draft, Writing – review & editing.

Declaration of competing interest

The authors declare that they have no known competing financial interests or personal relationships that could have appeared to influence the work reported in this paper.

Funding

This research did not receive any specific grant from funding agencies in the public, commercial, or not-for-profit sectors.

References

Abancó, C., Bennett, G.L., Matthews, A.J., Matera, M.A.M., Tan, F.J., 2021. The role of geomorphology, rainfall and soil moisture in the occurrence of landslides triggered by 2018 Typhoon Mangkhut in the Philippines. Nat. Hazards Earth Syst. Sci. 21, 1531–1550. https://doi.org/10.5194/nhess-21-1531-2021

Abancó, C., Jones, J.N., 2023. Areas affected by landslides following Typhoon Mangkhut in Itogon, Philippines, September 2018 [dataset]. NERC EDS Environmental Information Data Centre. https://doi.org/10.5285/32765a61-8510-4dfc-b7c7-58bad12f8497

Bartos, M., et al., 2024. mdbartos/pysheds [software]. Zenodo. https://doi.org/10.5281/zenodo.3822494 (version 0.5 used)

Behling, R., Roessner, S., Kaufmann, H., Kleinschmit, B., 2014. Automated spatiotemporal landslide mapping over large areas using RapidEye time series data. Remote Sens. 6, 8026–8055. https://doi.org/10.3390/rs6098026

Belair, G.M., Jones, E.S., Luna, L.V., Mirus, B.B., 2019. Landslide Inventories across the United States (ver. 3.0, February 2025) [dataset]. U.S. Geological Survey data release. https://doi.org/10.5066/P14AJF8I

Brenning, A., 2005. Spatial prediction models for landslide hazards: review, comparison and evaluation. Nat. Hazards Earth Syst. Sci. 5, 853–862. https://doi.org/10.5194/nhess-5-853-2005

Brown, C.F., Kazmierski, M.R., Pasquarella, V.J., Rucklidge, W.J., Samsikova, M., Zhang, C., et al., 2025. AlphaEarth Foundations: An embedding field model for accurate and efficient global mapping from sparse label data. arXiv:2507.22291. https://doi.org/10.48550/arXiv.2507.22291

Burgi, P.M., Toney, L.D., Collins, E.A., Murphy, C.R., Ellison, S.M., Schmitt, R.G., Allstadt, K.E., et al., 2025. Preliminary landslide inventory for landslides triggered by Hurricane Helene (September 2024) [dataset]. U.S. Geological Survey data release. https://doi.org/10.5066/P14CHGKS

Cheng, Y., Zhu, Q., Fan, L., 2026. From landslide conditioning factors to satellite embeddings: Evaluating the utilisation of Google AlphaEarth for landslide susceptibility mapping using deep learning. arXiv:2601.07268 (v2). https://doi.org/10.48550/arXiv.2601.07268

Cornes, R.C., van der Schrier, G., van den Besselaar, E.J.M., Jones, P.D., 2018. An ensemble version of the E-OBS temperature and precipitation data sets. J. Geophys. Res. Atmos. 123, 9391–9409. https://doi.org/10.1029/2017JD028200

Daly, C., Halbleib, M., Smith, J.I., Gibson, W.P., Doggett, M.K., Taylor, G.H., Curtis, J., Pasteris, P.P., 2008. Physiographically sensitive mapping of climatological temperature and precipitation across the conterminous United States. Int. J. Climatol. 28, 2031–2064. https://doi.org/10.1002/joc.1688

DerSimonian, R., Laird, N., 1986. Meta-analysis in clinical trials. Control. Clin. Trials 7, 177–188. https://doi.org/10.1016/0197-2456(86)90046-2

Du, Y., Zheng, T., Yang, P., Li, Y., Zhou, J., Yang, K., 2026. Code, analysis log and derived data for "Post-event information in calendar-year satellite products inflates landslide susceptibility assessments" (Version 1.0) [dataset]. Zenodo. https://doi.org/10.5281/zenodo.23467612

ESA (European Space Agency), 2022. Copernicus DEM (GLO-30) [dataset]. https://doi.

org/10.5270/ESA-c5d3d65

Fang, C., Fan, X., Wang, X., Nava, L., Zhong, H., et al., 2024. A globally distributed dataset of coseismic landslide mapping via multi-source high-resolution remote sensing images. Earth Syst. Sci. Data 16, 4817–4842. https://doi.org/10.5194/essd-16-4817-2024

Fang, J., Luo, W., Huang, Q., Li, W., Chen, Y.-C., Liu, C.-C., 2026. Annual geospatial foundation model embeddings for landslide susceptibility assessment in Taiwan. npj Nat. Hazards (article in press, published online 16 September 2026). https://doi.org/10.1038/s44304-026-00268-7

Fell, R., Corominas, J., Bonnard, C., Cascini, L., Leroi, E., Savage, W.Z., 2008. Guidelines for landslide susceptibility, hazard and risk zoning for land use planning. Eng. Geol. 102, 85–98. https://doi.org/10.1016/j.enggeo.2008.03.022

Feng, Z., Atzberger, C., Jaffer, S., Knezevic, J., Sormunen, S., Young, R., et al., 2025. TESSERA: Temporal embeddings of surface spectra for Earth representation and analysis. arXiv:2506.20380. https://doi.org/10.48550/arXiv.2506.20380

Ferrario, M.F., 2023. Inventory of landslides triggered by heavy rainfall in the Emilia-Romagna region (Italy) in May 2023 [dataset]. Zenodo. https://doi.org/10.5281/zenodo.8102429

Ferrario, M.F., Livio, F., 2024. Rapid mapping of landslides induced by heavy rainfall in the Emilia-Romagna (Italy) region in May 2023. Remote Sens. 16, 122. https://doi.org/10.3390/rs16010122

Guzzetti, F., Reichenbach, P., Ardizzone, F., Cardinali, M., Galli, M., 2006. Estimating the quality of landslide susceptibility models. Geomorphology 81, 166–184. https://doi.org/10.1016/j.geomorph.2006.04.007

Guzzetti, F., Mondini, A.C., Cardinali, M., Fiorucci, F., Santangelo, M., Chang, K.-T., 2012. Landslide inventory maps: New tools for an old problem. Earth-Sci. Rev. 112, 42–66. https://doi.org/10.1016/j.earscirev.2012.02.001

Hartung, J., Knapp, G., 2001. A refined method for the meta-analysis of controlled clinical trials with binary outcome. Stat. Med. 20, 3875–3889. https://doi.org/10.1002/sim.1009

IntHout, J., Ioannidis, J.P.A., Borm, G.F., 2014. The Hartung-Knapp-Sidik-Jonkman method for random effects meta-analysis is straightforward and considerably outperforms the standard DerSimonian-Laird method. BMC Med. Res. Methodol. 14, 25. https://doi.org/10.1186/1471-2288-14-25

Jin, J., Chen, G., 2025. The coseismic landslides induced by 2023 Jishishan earthquake [dataset]. Zenodo. https://doi.org/10.5281/zenodo.15791003

Juang, C.S., Stanley, T.A., Kirschbaum, D.B., 2019. Using citizen science to expand the global map of landslides: Introducing the Cooperative Open Online Landslide Repository (COOLR). PLoS ONE 14, e0218657. https://doi.org/10.1371/journal.pone.0218657

Kapoor, S., Narayanan, A., 2023. Leakage and the reproducibility crisis in machine-learning-based science. Patterns 4, 100804. https://doi.org/10.1016/j.patter.2023.100804

Karasiak, N., Dejoux, J.-F., Monteil, C., Sheeren, D., 2022. Spatial dependence between training and test sets: another pitfall of classification accuracy assessment in remote sensing. Mach. Learn. 111, 2715–2740. https://doi.org/10.1007/s10994-021-05972-1

Kaufman, S., Rosset, S., Perlich, C., Stitelman, O., 2012. Leakage in data mining: Formulation, detection, and avoidance. ACM Trans. Knowl. Discov. Data 6, 15. https://doi.org/10.1145/2382577.2382579

Ke, G., Meng, Q., Finley, T., Wang, T., Chen, W., Ma, W., Ye, Q., Liu, T.-Y., 2017. LightGBM: A highly efficient gradient boosting decision tree. In: Advances in Neural Information Processing Systems 30, pp. 3146–3154.

Knezevic, J., Atzberger, C., Feng, Z., Pellegrini, A.F.A., Keshav, S., Coomes, D., 2026. Annual Earth-observation embeddings encode wildfire disturbance and support simplified burned area mapping. arXiv:2609.25731. https://doi.org/10.48550/arXiv.2609.25731

Lakens, D., 2017. Equivalence tests: A practical primer for t tests, correlations, and meta-analyses. Soc. Psychol. Personal. Sci. 8, 355–362. https://doi.org/10.1177/1948550617697177

Li, M., Li, W., Liu, H., Liang, C., 2026. Leveraging geospatial foundation model embeddings for local-scale landslide susceptibility mapping via positive-unlabeled learning. Research Square preprint. https://doi.org/10.21203/rs.3.rs-10786241/v1

Liu, H., Xu, Y., Hu, G., Yuan, R., Zhao, X., Tang, J., Lu, L., Xu, W., 2025. Characteristics of earthquake-triggered landslides under high terrain undulation landscapes: a case study of the secondary effects of the 5 September 2022 Ms 6.8 Luding earthquake, SW China. J. Geol. Soc. 182, jgs2024-253. https://doi.org/10.1144/jgs2024-253 (inventory: https://doi.org/10.6084/m9.figshare.28944505.v1)

Liu, W., Li, S., Shi, C., Zhu, H., Huang, C., Yin, L., 2026. Landslide mapping and susceptibility assessment in the middle and lower reaches of the Nujiang River (2017–2025) using satellite embedding and multidimensional environmental factors. Remote Sens. 18, 1854. https://doi.org/10.3390/rs18111854

Lombardo, L., Tanyas, H., 2020. Chrono-validation of near-real-time landslide susceptibility models via plug-in statistical simulations. Eng. Geol. 278, 105818. https://doi.org/10.1016/j.enggeo.2020.105818

Mancino, S., Sblano, A., Lovergine, F.P., Massimi, V., Sethi, T., et al., 2025. Unified Global Landslide Catalogue (UGLC): A single, standardised global-scale landslide dataset. Earth Syst. Sci. Data Discuss. https://doi.org/10.5194/essd-2025-482 (dataset: https://doi.org/10.5281/zenodo.18643456)

Maus, V., Giljum, S., da Silva, D.M., Gutschlhofer, J., da Rosa, R.P., Luckeneder, S., et al., 2022. An update on global mining land use. Sci. Data 9, 433. https://doi.org/10.1038/s41597-022-01547-4 (dataset: https://doi.org/10.1594/PANGAEA.942325)

Merghadi, A., Yunus, A.P., Dou, J., Whiteley, J., ThaiPham, B., Bui, D.T., et al., 2020. Machine learning methods for landslide susceptibility studies: A comparative overview of algorithm performance. Earth-Sci. Rev. 207, 103225. https://doi.org/10.1016/j.earscirev.2020.103225

Pizziolo, M., Berti, M., Scaroni, M., Generali, M., Critelli, V., Mulas, M., et al., 2024. RER2023: the landslide inventory dataset of the May 2023 Emilia-Romagna event – Version 1 [dataset]. Zenodo. https://doi.org/10.5281/zenodo.13742643

Ploton, P., Mortier, F., Réjou-Méchain, M., Barbier, N., Picard, N., et al., 2020. Spatial validation reveals poor predictive performance of large-scale ecological mapping models. Nat. Commun. 11, 4540. https://doi.org/10.1038/s41467-020-18321-y

Reichenbach, P., Rossi, M., Malamud, B.D., Mihir, M., Guzzetti, F., 2018. A review of statistically-based landslide susceptibility models. Earth-Sci. Rev. 180, 60–91. https:

//doi.org/10.1016/j.earscirev.2018.03.001

Roberts, D.R., Bahn, V., Ciuti, S., Boyce, M.S., Elith, J., et al., 2017. Cross-validation strategies for data with temporal, spatial, hierarchical, or phylogenetic structure. Ecography 40, 913–929. https://doi.org/10.1111/ecog.02881

Samia, J., Temme, A., Bregt, A., Wallinga, J., Guzzetti, F., Ardizzone, F., Rossi, M., 2017. Do landslides follow landslides? Insights in path dependency from a multi-temporal landslide inventory. Landslides 14, 547–558. https://doi.org/10.1007/s10346-016-0739-x

Samia, J., Temme, A., Bregt, A., Wallinga, J., Guzzetti, F., Ardizzone, F., 2020. Dynamic path-dependent landslide susceptibility modelling. Nat. Hazards Earth Syst. Sci. 20, 271–285. https://doi.org/10.5194/nhess-20-271-2020

Scheip, C.M., Wegmann, K.W., 2021. HazMapper: a global open-source natural hazard mapping application in Google Earth Engine. Nat. Hazards Earth Syst. Sci. 21, 1495–1511. https://doi.org/10.5194/nhess-21-1495-2021

Schuirmann, D.J., 1987. A comparison of the two one-sided tests procedure and the power approach for assessing the equivalence of average bioavailability. J. Pharmacokinet. Biopharm. 15, 657–680. https://doi.org/10.1007/BF01068419

Steger, S., Schmaltz, E., Glade, T., 2020. The (f)utility to account for pre-failure topography in data-driven landslide susceptibility modelling. Geomorphology 354, 107041. https://doi.org/10.1016/j.geomorph.2020.107041

Thasma, S., Ho, Y.-H., Mostafavi, A., 2026. Beyond backscatter: AlphaEarth land-cover priors for rapid SAR flood segmentation across foundation backbones. arXiv:2606.29134. https://doi.org/10.48550/arXiv.2606.29134

Trigila, A., Iadanza, C., Spizzichino, D., 2010. Quality assessment of the Italian Landslide Inventory using GIS processing. Landslides 7, 455–470. https://doi.org/10.1007/s10346-010-0213-0

Viechtbauer, W., 2005. Bias and efficiency of meta-analytic variance estimators in the random-effects model. J. Educ. Behav. Stat. 30, 261–293. https://doi.org/10.3102/10769986030003261

Xu, C., Xu, X., Shyu, J.B.H., 2015. Database and spatial distribution of landslides triggered by the Lushan, China Mw 6.6 earthquake of 20 April 2013. Geomorphology 248, 77–92. https://doi.org/10.1016/j.geomorph.2015.07.002 (inventory: https://doi.org/10.5066/F7KS6Q2P)

Yunus, A.P., Fan, X., Tang, X., Jie, D., Xu, Q., Huang, R., 2020. Decadal vegetation succession from MODIS reveals the spatio-temporal evolution of post-seismic landsliding after the 2008 Wenchuan earthquake. Remote Sens. Environ. 236, 111476. https://doi.org/10.1016/j.rse.2019.111476

Zanaga, D., Van De Kerchove, R., Daems, D., De Keersmaecker, W., et al., 2022. ESA WorldCover 10 m 2021 v200 [dataset]. Zenodo. https://doi.org/10.5281/zenodo.7254221

Zhang, S., Li, R., Wang, F., Iio, A., 2019. Characteristics of landslides triggered by the 2018 Hokkaido Eastern Iburi earthquake, Northern Japan. Landslides 16, 1691–1708. https://doi.org/10.1007/s10346-019-01207-6 (inventory: https://doi.org/10.5281/zenodo.2577300)

Zhuang, Y., Hobeichi, S., Shi, P., Huang, F., 2026. Evaluating AlphaEarth Foundations embeddings for wildfire susceptibility mapping. arXiv:2608.12663. https://doi.org/10

.48550/arXiv.2608.12663

Supplementary material for

Post-event information in calendar-year satellite products inflates landslide susceptibility assessments

Yifan Du, Tianhe Zheng, Peiyan Yang, Yibo Li, Junhang Zhou, Kun Yang

North China University of Water Resources and Electric Power, 136 Jinshui East Road, Zhengzhou 450046, Henan, China

Text S1. Joint dose–response model and recovery adjustment

Data. For event i and model k, the model uses the full-sample point estimates of the event-year increment d_0 = AUC(Y) − AUC(Y−1) and the year-after increment d_1 = AUC(Y+1) − AUC(Y−1). Their 2 × 2 covariance matrix Σ comes from the same 1,000 joint spatial-cluster bootstrap resamples that were used for the audit. The two increments share AUC(Y−1) and are positively correlated (median correlation 0.78 for the patch model and 0.87 for the point model).

Model. $d_1 = \mu + e_1$ and $d_0 = r\,\mu + e_0$, with $(e_0, e_1) \sim \mathrm{N}(0, \Sigma)$. The terms are:

- $\mu \sim \mathrm{N}(m, \omega^2)$: the event's fully post-event increment;
- $r = A\,g(f) + \eta$, with $\eta \sim \mathrm{N}(0, \tau^2)$: the dose–response with event-level scatter;
- $g(f) = 1/[1 + \exp(-(f - f_{50})/s)]$.

The parameters are constrained to $A > 0$, $0 < f_{50} < 1$ and $0.01 \le s \le 0.5$. The ratio r is integrated analytically, which adds $\tau^2\mu^2$ to the variance of d_0. μ is integrated with 40-node Gauss–Hermite quadrature.

Estimation and tests.

- Maximum marginal likelihood (Nelder–Mead, eight starting points, each refined once).
- The slope test compares $r = a + b\,f + \eta$ with a constant ratio by a likelihood-ratio test; the one-sided p-value is half the χ^2_1 tail when $b > 0$.
- The interval for f_{50} is the profile-likelihood interval on a grid from 0.02 to 0.80. Bounds at the grid edges are written as ≤ 0.02 or ≥ 0.80.
- Robustness checks: an event bootstrap of between-model differences, leave-one-event-out refits, and an exponential saturation curve.

Recovery adjustment. The year-after product covers lags f to $f + 1$ years. With exponential recovery at rate λ, its signal is proportional to $\exp(-\lambda f)$, so the ratio d_0/d_1 contains a factor $\exp(\lambda f)$. We estimated λ from the products of the year after next (Y+2, 17 events) as $\lambda = -\ln q$, with $q = \Sigma d_2/\Sigma d_1$ over events whose year-after increment is distinguishable from zero. The interval for q comes from an event bootstrap with 2,000 resamples. We then refitted the joint model with d_1 multiplied by $\exp(\lambda f)$, its variance by $\exp(2\lambda f)$ and the covariance by $\exp(\lambda f)$.

Quantity	Point LightGBM	Patch CNN2D
Decay ratio q (event bootstrap 95% CI)	0.770 (0.661–0.854)	0.762 (0.592–0.898)
λ (per year)	0.26	0.27
Unadjusted: slope p; A; f_{50}	0.0005; 1.16; 0.24	0.0003; 1.14; 0.26

Quantity	Point LightGBM	Patch CNN2D
Adjusted: slope p; A; f_{50}	0.004; 0.96; 0.23	0.002; 0.99; 0.26
Adjusted with λ at the CI ends: slope p; A	0.002–0.013; 0.87–1.03	0.001–0.011; 0.87–1.08

Fixed-window reference (Sentinel-2). For the composites, we replaced d_1 by d_{fix} = AUC(composite of the 12 months after the event day) − AUC(Y−1). All windows were computed from the same scenes with the same code, and the point model used the nine channels of the centre 30 m cell.

Model	Calendar year-after reference	Fixed 12-month reference
Point LightGBM	slope p = 0.004; f_{50} 0.33; τ 0.70	slope p = 0.0006; f_{50} 0.34; A 0.96; τ 0.23
Patch CNN2D	slope p = 0.004; f_{50} 0.32; τ 0.65	slope p = 0.011 (logistic fit nearly linear); τ 0.24

Text S2. Survey of studies that use annual embeddings for dated hazards

A web search on 10 October 2026 combined the terms AlphaEarth, satellite embedding, Google Satellite Embedding, AEF and embedding field with landslide, wildfire, flood, hazard and susceptibility. It covered arXiv, Research Square, ESS Open Archive and journal websites and was followed by backward citation checks. For each study we read the methods and coded the temporal relation between the embeddings and the labels.

Four studies of dated-hazard susceptibility or prediction gave input years that could be verified. Cheng et al. (2026) used embeddings of the same year as the events, or a cumulative inventory with a single embedding year. Li et al. (2026) used a multi-year mean that covers the event years. Zhuang et al. (2026) used a multi-year mean or sequence that covers the fire years. Fang et al. (2026) used the previous year. Two further studies could not be coded, and post-event mapping studies were listed separately.

Fang et al. (2026), verified against the full text. We read the accepted manuscript (article in press, published online 16 September 2026). The study predicts pixels newly mapped in the year-t annual landslide inventory of Taiwan (2017–2024) from AlphaEarth embeddings of year $t - 1$, with expanding-window temporal validation and two spatial hold-out schemes. It reports a mean one-year-ahead ROC-AUC of 0.956 and a capture of 89.9–95.0% of future landslide area in the top 5% of the island in 2019–2023, with lower skill in 2024. Its decomposition by failure history is independent evidence for Sect. 4.4 of the main text. In 2020–2023, 63–68% of the newly mapped area lay on pixels present in an earlier inventory. These reactivated pixels were predicted with ROC-AUC 0.978–0.984, against 0.866–0.938 for isolated first-observed pixels (0.791 in 2024). The authors also note that the annual inventories are release-year snapshots whose imagery can extend into the next year. Labels newly mapped in year t can therefore include failures that occurred late in year $t - 1$, which a year-$t - 1$ product partly records; Text S5 gives a rough bound for this design.

Text S3. Time-stamped analysis log and deviations from the prespecified designs

The time-stamped analysis log (in Chinese) records every design and criterion before computation, with time stamps. Entries from 8 October onwards were written on the analysis server in UTC; the two entries of 4 October were written on a local machine in UTC−7 and are converted to UTC in the tables below. None of its entries was deposited with a third party; we therefore call the analyses prespecified. A copy of the log, from which entries unrelated to the analyses (server administration, file sharing and manuscript preparation)

were removed, is archived with the code and data (https://doi.org/10.5281/zenodo.23467612). The table lists its main entries; those of 16 October 2026 are follow-up analyses added after internal review of a first draft of this paper:

Time (UTC, 2026)	Entry
4 Oct 12:43	Event list frozen (logged as 05:43 local time, UTC−7)
4 Oct 14:08	Three transition-zone events added, with a prediction (logged as 07:08 local time, UTC−7)
8 Oct 13:14–16:15	Re-analysis of Cheng et al.; patch-level audit; Sentinel-2 patch composites
10 Oct ≈10:32	Joint dose–response; whole-region maps; literature survey protocol
10 Oct 11:41	Autumn-rainfall prediction frozen (SHA-256 prefix f95c07a37e1db2ad)
14 Oct 10:31	Maps for eight further events
14 Oct 16:07–17:14	TESSERA audit; clear-sky dose; inventory timing; vegetation recovery
15 Oct 00:09–00:54	Phenology-corrected inventory timing; composite-weighted dose; North Carolina forward test
16 Oct ≈03:23	Follow-up analyses: recovery adjustment from the year after next; fixed-window Sentinel-2 reference; training-year × prediction-year decomposition; placebo-corrected increments; REML–HKSJ re-pooling; temporal and spatial independence of the forward tests; scar-direction projection; Mangkhut and mining; Lushan forward test (all criteria in Table S10)
16 Oct 11:28	Second follow-up: sensitivity of the equivalence tests to the margin (Table S17); data-version manifests (Table S18, Data S1–S2); figure updates

Deviations and corrections, all recorded in the log when they occurred:

1. **Patch-level audit design.** The audit switched from a block-budget subset to all audit points, and its valid-point rule was aligned with the point-level audit. Both changes were made before any patch result.
2. **Corrupted cache block.** One cached AlphaEarth block had a band filled with no-data. It was re-downloaded, and a cross-band mask check was added.
3. **Sentinel-2 indices.** These were clipped to [−1, 1] per scene, because the −0.1 offset makes dark reflectances negative.
4. **Neighbouring-zone windows.** 2,901 Emilia-Romagna points received neighbouring-zone windows (amended before the affected results).
5. **Point inventory.** A point-inventory mode was added to the sample builder for Helene, and all blocks were used because the budget did not bind.
6. **Helene land cover.** A WorldCover tile was replaced by a local copy; values were identical where the remote read had succeeded.
7. **Early statement corrected.** A CPU-stage statement about the Cheng et al. setting, based on simplified networks, was corrected after the full re-analysis.
8. **Superseded half-saturation estimate.** A patch-level f_{50} of 0.16 from the ratio method was superseded by the joint model.
9. **Discarded timing method.** The first inventory-timing method failed its own check and was replaced by the phenology-corrected method.
10. **Two exploratory explanations withdrawn.** "A different TESSERA production batch in 2024" and "faster tropical recovery" were not supported.
11. **pysheds.** Version 0.5 was installed in a temporary container for the upslope area of the North Carolina and Lushan forward tests; neither the host nor the image was changed.
12. **Log time of the first follow-up.** It was first recorded as 03:30 and corrected to about 03:23 from file times. The first follow-up computation started at about 03:25.
13. **Fixed-window Sentinel-2 predictions.** In the fixed-window analysis, the centre-cell LightGBM and patch-model runs wrote to the same file. The deterministic LightGBM predictions were recomputed after the patch-model run finished.

14. **Bootstrap seeds in the forward tests.** The Emilia-Romagna and North Carolina forward tests were recomputed in the follow-up analyses with a bootstrap seeded per subset. Point estimates are full-sample values; they differ from the initial run (Table S5) by at most 0.002 (for example, F1 − L = −0.076 rather than −0.075).
15. **Lushan static factors.** The prespecified static factors of the Lushan forward test include log upslope area, which the first run omitted. The omission was found while the follow-up results were being checked against the prespecified designs; the correction was written into the log before recomputation (16 Oct 06:51). With the prespecified factors, F1 − L was +0.024 (−0.025 to 0.071) instead of +0.031 (−0.019 to 0.080), and the classification (undecided) did not change. Contrasts between embedding scenarios are unaffected. The main text and Fig. 7 use the prespecified version; Table S14 lists both.
16. **Log time of the second follow-up.** Its entry was first stamped 11:40 and corrected within minutes to its actual writing time, 11:28, before any of its computations.

Text S4. Data sources, processing details and code index

Data sources and processing

AlphaEarth Satellite Embedding V1 (annual).

- Source: the Source Cooperative mirror `tge-labs/aef/v1/annual`, accessed October 2026.
- Download: blocks of 1,024 × 1,024 pixels with 64 bands, fetched with byte-range requests.
- Checks: HTTP 206 with the exact length; zstd decoding; ≥ 99.9% of valid pixels with a de-quantized norm between 0.9 and 1.1; identical masks across bands.
- The follow-up analyses added the products of the year after next (Y+2) for 17 events: 457 blocks, 18.5 GB, no integrity failures.

TESSERA v1 and v1.1-cam. From Source Cooperative `tessera/tessera`, read by range requests. Version v1 was used for Emilia-Romagna, Fujian, Helene, Jishishan, Luding, Lushan and Mesetas, and v1.1-cam for Agatha, Freddy and São Paulo (and for a version-sensitivity check of Mesetas).

Data versions. On 16 October 2026 we sent an HTTP HEAD request for every source file behind the data we used. We recorded each file's ETag, size and last-modified date (Table S18; full lists in Supplementary Data S1 and S2). All 291 AlphaEarth files and all 3,952 TESSERA files answered with status 200, and all had last been modified before we read them. The SHA-256 hashes of the local index files and of both lists are given in Table S18.

Sentinel-2 Level-2A. From the Earth Search STAC catalogue.

Other inputs. Copernicus GLO-30; ESA WorldCover 2021; E-OBS; PRISM.

Inventories added in the follow-up analyses.

- The 2013 Lushan inventory (Xu et al., 2015; USGS ScienceBase doi:10.5066/F7KS6Q2P). It has 15,546 point features; the file checksums matched the repository.
- The global mining polygons v2 (Maus et al., 2022).
- OpenStreetMap mining features around Itogon (via the Overpass API).

Code index

Paths are relative to the project repository.

Initial analyses (4–15 October 2026):

- `scripts/m3_build_event_points.py`
- `scripts/m3_g4_patches.py`
- `mvp/m3_g4_patch_audit.py`
- `mvp/m3_h1_dose_joint.py`
- `mvp/m3_h2_maps.py`
- `mvp/m3_j3_maps.py`
- `scripts/m3_t_tessera.py`, `mvp/m3_t_audit.py`
- `scripts/m3_g3_s2_patches.py`, `mvp/m3_g3_patch_compare.py`
- `mvp/m3_s_dose_all.py`
- `mvp/m3_g1_exp0_gpu.py`
- `mvp/m3_expD_forward.py`
- `scripts/m3_d2_*.py`, `mvp/m3_d2_forward.py`
- `mvp/m3_k_analysis.py`, `mvp/m3_m2_dating.py`, `mvp/m3_r_recovery.py`, `mvp/m3_expC_mechanism.py`, `mvp/m3_expB2_windows.py`
- `mvp/m3_paper_numbers.py`, `mvp/m3_paper_figs.py`

Follow-up analyses (16 October 2026):

Analysis	Code	Output
Shared statistics (DL, REML–HKSJ, TOST)	`mvp/m3_v2_stats.py`	—
Placebo-corrected increments, REML–HKSJ	`mvp/m3_v2_robust.py`	`mvp/m3_v2_robust.csv`
Training-year × prediction-year decomposition	`mvp/m3_v2_decomp.py`	`mvp/m3_v2_decomp.csv`
Year after next and recovery adjustment	`scripts/m3_v2_y2.py`	`mvp/m3_v2_y2.csv`, `mvp/m3_v2_y2_log.txt`
Fixed-window Sentinel-2 reference	`scripts/m3_v2_s2window.py`	`mvp/m3_v2_s2window.csv`
Forward-test robustness and scar direction	`mvp/m3_v2_forward.py`	`mvp/m3_v2_forward.csv`
Lushan forward test	`scripts/m3_v2_lushan_prepare.py`, `scripts/m3_v2_lushan_loga.py`, `mvp/m3_v2_lushan_forward.py loga`	`mvp/m3_v2_lushan_loga.csv` (prespecified static factors); `mvp/m3_v2_lushan.csv` (first run, without log upslope area)
Mangkhut and mining	`mvp/m3_v2_mangkhut.py`	`mvp/m3_v2_mangkhut.csv`
Tables S11–S16	`mvp/m3_paper_tables_v2.py`	`mvp/m3_paper_tables_v2.md`
Figures 1–7	`mvp/m3_paper_figs_v2.py`	`mvp/figs/paper_v2_fig*.png`
Equivalence-margin sensitivity (Table S17)	`mvp/m3_v3_tost_margins.py`	`mvp/m3_v3_tost_margins.csv`
Data-version manifests (Table S18, Data S1–S2)	`scripts/m3_v3_manifest.py`	`datasets/derived/m3_events/v3/*_manifest.csv`
Figures 3, 4, 5 and 7 (final panels)	`mvp/m3_paper_figs_v3.py` (options of `mvp/m3_paper_figs_v2.py`)	`mvp/figs/paper_v3_fig*.png`

Environment. Python 3.10.12, NumPy 2.2.6, SciPy 1.15.3, scikit-learn 1.7.2, LightGBM 4.7.0, PyTorch 2.11.0 (CUDA 12.8), in a Docker image. Versions are listed in `scripts/docker_gpu/requirements.lock.txt`.

Text S5. Rough bound for designs based on annual inventories

When a share s of a year-Y inventory occurred late in year Y−1, the inflation of a previous-year design is approximately $s \times r(f) \times D$. Here $D = 0.104$ is the median year-after increment. The bound is below 0.01–0.02 AUC in typical cases; for example, it is 0.022 when 20% of the inventory dates from the previous summer.

Text S6. Further mechanism diagnostics

Non-landslide disturbance (Emilia-Romagna). The Ferrario (2023) inventory also maps river-bank and field-damage polygons. We sampled 2,252 points in these polygons, 15,000 landslide crowns and 15,000 undisturbed points more than 100 m from any mapped polygon.

- **Embedding change.** The year-to-year change (1 − cosine similarity, median) between 2022 and 2023 was 0.074 at disturbed points, 0.048 at landslide crowns and 0.042 at undisturbed points. Between 2021 and 2022 it was 0.024–0.031.
- **Classification.** A model trained to separate landslides from undisturbed points (spatial 5-fold CV, 500 m buffer) also scored the disturbed points as more landslide-like when it used the event-year product. The AUC of disturbed against undisturbed points was 0.70 with the 2022 product and 0.75 with the 2023 product; restricted to slopes of 5–35°, it was 0.71 and 0.79. Without an event, it changed little (0.69 → 0.70 between 2021 and 2022).

Scar direction in the forward tests. For each forward region we took the mean change of the test embeddings between Y−1 and Y at the test landslides, minus that at the test controls, and normalized it. We then projected the Y−1 embeddings of the training points onto this direction. Two predictions were prespecified. The projection would separate earlier landslides from their controls (AUC > 0.5) in both regions, and it would do so more strongly in North Carolina than in Emilia-Romagna, matching the order of their prediction-time increments. Both held (projection AUC 0.645 and 0.595). At the test landslides, the change of the clean-model score between Y−1 and Y inputs correlated with the change of the projection (Spearman +0.18 in North Carolina, +0.11 in Emilia-Romagna). At the test controls the correlation was +0.01 and +0.12, so the evidence is stronger in North Carolina. An exploratory split of the North Carolina training records by date did not follow the expected ordering, in which a higher projection AUC goes with a larger increment. Records dated up to 2010 gave a prediction-time increment of +0.060 (projection AUC 0.692); records dated from 2011 (527 landslides) gave +0.030 (projection AUC 0.806). The projection AUC is therefore not a quantitative predictor of the size of the increment. Training on Y and predicting with Y−1 (F4) changed the AUC by −0.014 in North Carolina, +0.034 in Emilia-Romagna and +0.028 in Lushan (Table S14).

Clear-sky weighting. Calendar time explained the dose better than the share of clear Sentinel-2 observations after the event. Replacing f by f_{clear} raised the negative log-likelihood by 2.68 (patch) and 1.87 (point) over 17 events (Table S9). For Mangkhut, $f_{\text{clear}} = 0.32$ against $f = 0.29$. For the composites themselves, weighting by the observations that entered the composite did not improve the fit either; this test had little power.

Visibility. AlphaEarth year-after increments correlated with the year-after NDVI decline at the landslides across 15 events (patch model: Spearman 0.61, $p = 0.016$; point model: 0.47, $p = 0.074$). For Agatha, however, the NDVI barely changed (−0.005) while d_1 was 0.114.

Inventory timing (Mangkhut). Phenology-corrected NDVI dating classified 22.8% of the detected Mangkhut declines as pre-typhoon. The method check on Iburi gave 9.6%, against a limit of 10%. Account-

ing for this timing raised the predicted ratios from 0.78 to 0.87 (patch) and from 0.58 to 0.70 (point), still below the observed 1.52 and 0.97.

Mining (Mangkhut). The mapped mining area within the inventory hull plus 5 km is 0.63 km^2: one polygon of the global dataset (0.15 km^2) and 13 OpenStreetMap features. Excluding points within 500 m or 1 km removed 42–116 landslides. The point-model ratio fell to 0.85–0.89, but the patch-model ratio stayed at 1.26–1.48 (Table S15).

Supplementary tables

Table S1. Per-event results of the AlphaEarth audit (18 events). Increments are paired AUC differences with spatial-cluster bootstrap 95% CIs. The increments shown are bootstrap means; the ratio d_0/d_1 is the ratio of the full-sample increments, as used by the joint model and Fig. 4, and is unstable when d_1 is small.

Event	f	Model	AUC Y−1	Event year (Y − Y−1)	Placebo (Y−1 − Y−2)	Year after (Y+1 − Y−1)	Ratio d0/d1
Mesetas (Colombia)	0.02	LightGBM	0.855	+0.007 (−0.006, +0.019)	+0.022 (+0.009, +0.036)	+0.090 (+0.070, +0.111)	0.07
	0.02	CNN2D	0.878	+0.020 (+0.007, +0.033)	+0.010 (−0.005, +0.026)	+0.081 (+0.066, +0.097)	0.25
Jishishan (China)	0.04	LightGBM	0.591	+0.025 (+0.004, +0.048)	+0.020 (+0.008, +0.032)	+0.026 (+0.003, +0.053)	0.99
	0.04	CNN2D	0.734	−0.017 (−0.056, +0.016)	−0.027 (−0.059, −0.002)	+0.039 (+0.011, +0.070)	−0.44
Nalgae, Mindanao (Philippines)	0.18	LightGBM	0.804	+0.037 (+0.016, +0.064)	+0.012 (−0.009, +0.036)	+0.016 (−0.010, +0.045)	2.13
	0.18	CNN2D	0.768	−0.013 (−0.044, +0.015)	+0.031 (+0.004, +0.061)	−0.026 (−0.055, −0.002)	0.61
Helene, southern Appalachians (USA)	0.26	LightGBM	0.815	+0.074 (+0.064, +0.084)	−0.005 (−0.011, +0.001)	+0.126 (+0.109, +0.146)	0.59
	0.26	CNN2D	0.801	+0.065 (+0.055, +0.078)	−0.010 (−0.020, −0.002)	+0.130 (+0.114, +0.148)	0.50
Palu (Indonesia)	0.26	LightGBM	0.720	+0.116 (+0.081, +0.154)	—	+0.258 (+0.214, +0.298)	0.45
	0.26	CNN2D	0.737	+0.132 (+0.085, +0.177)	—	+0.211 (+0.155, +0.260)	0.63
Mangkhut, Itogon (Philippines)	0.29	LightGBM	0.818	+0.055 (+0.039, +0.069)	—	+0.057 (+0.041, +0.072)	0.97
	0.29	CNN2D	0.763	+0.106 (+0.057, +0.159)	—	+0.070 (+0.035, +0.103)	1.52
Eastern Iburi (Japan)	0.32	LightGBM	0.829	+0.099 (+0.075, +0.122)	—	+0.153 (+0.123, +0.190)	0.65
	0.32	CNN2D	0.830	+0.118 (+0.078, +0.156)	—	+0.153 (+0.112, +0.195)	0.77
Luding (China)	0.32	LightGBM	0.757	+0.084 (+0.066, +0.100)	−0.018 (−0.029, −0.008)	+0.136 (+0.109, +0.163)	0.61
	0.32	CNN2D	0.796	+0.106 (+0.085, +0.128)	−0.012 (−0.031, +0.006)	+0.133 (+0.110, +0.159)	0.80
Chittagong (Bangladesh)	0.38	LightGBM	0.808	+0.126 (+0.106, +0.148)	−0.002 (−0.010, +0.007)	+0.103 (+0.082, +0.126)	1.22
	0.38	CNN2D	0.804	+0.089 (+0.070, +0.110)	−0.004 (−0.015, +0.005)	+0.060 (+0.041, +0.080)	1.49
Northern Vietnam	0.41	LightGBM	0.678	+0.140 (+0.108, +0.173)	+0.013 (−0.004, +0.031)	+0.143 (+0.114, +0.182)	0.98
	0.41	CNN2D	0.721	+0.085 (+0.045, +0.120)	+0.027 (−0.017, +0.071)	+0.074 (+0.035, +0.110)	1.14
Fujian (China)	0.43	LightGBM	0.822	+0.070 (+0.050, +0.094)	−0.008 (−0.026, +0.008)	+0.076 (+0.046, +0.114)	0.92
	0.43	CNN2D	0.800	+0.025 (−0.005, +0.053)	−0.014 (−0.047, +0.020)	+0.016 (−0.016, +0.045)	1.52
Luzon (Philippines)	0.43	LightGBM	0.727	+0.200 (+0.178, +0.224)	+0.007 (−0.002, +0.016)	+0.219 (+0.193, +0.247)	0.91
	0.43	CNN2D	0.729	+0.203 (+0.179, +0.230)	+0.001 (−0.008, +0.012)	+0.210 (+0.184, +0.240)	0.97
Lushan (China)	0.58	LightGBM	0.833	+0.092 (+0.071, +0.115)	+0.003 (−0.007, +0.015)	+0.091 (+0.068, +0.115)	1.01
	0.58	CNN2D	0.842	+0.079 (+0.056, +0.106)	−0.003 (−0.014, +0.006)	+0.081 (+0.057, +0.110)	0.98
Agatha (Mexico)	0.59	LightGBM	0.766	+0.145 (+0.116, +0.172)	−0.010 (−0.024, +0.005)	+0.114 (+0.090, +0.137)	1.27
	0.59	CNN2D	0.789	+0.094 (+0.066, +0.119)	−0.010 (−0.030, +0.010)	+0.055 (+0.031, +0.077)	1.70
Emilia-Romagna (Italy)	0.63	LightGBM	0.908	+0.025 (+0.019, +0.031)	+0.000 (−0.004, +0.005)	+0.024 (+0.017, +0.031)	1.04
	0.63	CNN2D	0.935	+0.016 (+0.011, +0.021)	+0.002 (−0.001, +0.006)	+0.017 (+0.012, +0.023)	0.90
Freddy (Malawi)	0.81	LightGBM	0.853	+0.058 (+0.038, +0.079)	+0.009 (+0.000, +0.019)	+0.044 (+0.020, +0.069)	1.33
	0.81	CNN2D	0.833	+0.040 (+0.015, +0.064)	+0.009 (−0.005, +0.024)	+0.028 (+0.011, +0.046)	1.36
Pasaman, West Sumatra (Indonesia)	0.85	LightGBM	0.884	+0.090 (+0.058, +0.124)	+0.005 (−0.005, +0.016)	+0.076 (+0.046, +0.105)	1.18
	0.85	CNN2D	0.907	+0.054 (+0.030, +0.082)	−0.006 (−0.018, +0.004)	+0.037 (+0.019, +0.057)	1.45
São Paulo coast (Brazil)	0.86	LightGBM	0.791	+0.166 (+0.113, +0.228)	−0.022 (−0.043, −0.001)	+0.154 (+0.100, +0.220)	1.08
	0.86	CNN2D	0.798	+0.088 (+0.045, +0.141)	−0.004 (−0.023, +0.018)	+0.065 (+0.036, +0.092)	1.37

Table S2. TESSERA audit (10 events) with AlphaEarth recomputed on the same points, folds and bootstrap resamples.

Event	f	TESSERA version	Points (ls / all)	Pre-event AUC TESSERA / AE	TESSERA event year	TESSERA placebo	TESSERA year after	AlphaEarth event year	AE − TESSERA (event year)
Mesetas (Colombia)	0.02	v1	1,990 / 5,970	0.754 / 0.855	+0.020 (−0.002, +0.044)	+0.041 (+0.023, +0.062)	+0.127 (+0.095, +0.158)	+0.006 (−0.006, +0.019)	−0.014 (−0.035, +0.008)
Jishishan (China)	0.04	v1	2,984 / 8,660	0.537 / 0.541	+0.048 (+0.010, +0.080)	+0.016 (−0.001, +0.030)	+0.082 (+0.017, +0.148)	+0.020 (+0.000, +0.041)	−0.028 (−0.050, −0.002)
Helene, southern Appalachians (USA)	0.26	v1	2,213 / 6,639	0.706 / 0.815	+0.114 (+0.087, +0.154)	−0.007 (−0.022, +0.009)	+0.175 (+0.144, +0.214)	+0.073 (+0.064, +0.084)	−0.041 (−0.078, −0.013)
Luding (China)	0.32	v1	2,675 / 7,859	0.630 / 0.705	+0.066 (+0.047, +0.086)	+0.030 (+0.004, +0.050)	+0.144 (+0.102, +0.182)	+0.086 (+0.066, +0.102)	+0.019 (−0.000, +0.037)
Fujian (China)	0.43	v1	345 / 1,036	0.748 / 0.822	+0.125 (+0.087, +0.168)	−0.029 (−0.067, +0.006)	+0.107 (+0.074, +0.145)	+0.069 (+0.050, +0.094)	−0.056 (−0.100, −0.015)
Lushan (China)	0.58	v1	1,286 / 3,858	0.763 / 0.833	+0.113 (+0.092, +0.138)	−0.023 (−0.042, −0.004)	+0.103 (+0.081, +0.130)	+0.091 (+0.071, +0.115)	−0.022 (−0.042, −0.001)
Agatha (Mexico)	0.59	v1.1-cam	2,949 / 5,213	0.685 / 0.749	+0.182 (+0.148, +0.218)	−0.006 (−0.020, +0.008)	+0.165 (+0.137, +0.197)	+0.159 (+0.126, +0.197)	−0.023 (−0.053, +0.007)
Emilia-Romagna (Italy)	0.63	v1	3,000 / 9,000	0.814 / 0.897	+0.062 (+0.050, +0.075)	+0.011 (−0.004, +0.023)	+0.049 (+0.037, +0.063)	+0.031 (+0.023, +0.039)	−0.031 (−0.045, −0.020)
Freddy (Malawi)	0.81	v1.1-cam	1,634 / 4,582	0.735 / 0.853	+0.118 (+0.088, +0.143)	+0.011 (−0.010, +0.029)	+0.097 (+0.068, +0.122)	+0.058 (+0.038, +0.079)	−0.060 (−0.082, −0.035)
São Paulo coast (Brazil)	0.86	v1.1-cam	326 / 717	0.712 / 0.791	+0.227 (+0.171, +0.284)	−0.037 (−0.068, −0.000)	+0.173 (+0.118, +0.229)	+0.167 (+0.113, +0.228)	−0.060 (−0.108, −0.017)

Table S3. Sentinel-2 annual median composites versus AlphaEarth on the composite subset points (15 events). Point-model increments are shown without CIs for brevity.

Event	f	Points (ls / ctrl)	Pre-event AUC S2 / AE (patch)	S2 patch d0	AE patch d0	S2 point d0	AE point d0	AE − S2 (patch)
Mesetas (Colombia)	0.02	472 / 620	0.45 / 0.86	+0.087 (+0.004, +0.153)	−0.012 (−0.029, +0.005)	−0.078	−0.032	−0.099 (−0.167, −0.021)
Nalgae, Mindanao (Philippines)	0.18	56 / 112	0.57 / 0.75	−0.058 (−0.171, +0.049)	−0.033 (−0.086, +0.006)	−0.031	+0.010	+0.025 (−0.115, +0.153)
Palu (Indonesia)	0.26	332 / 677	0.41 / 0.52	+0.239 (+0.114, +0.367)	+0.123 (+0.034, +0.226)	+0.140	+0.096	−0.116 (−0.229, −0.004)
Eastern Iburi (Japan)	0.32	2,008 / 3,501	0.48 / 0.65	+0.125 (+0.063, +0.194)	+0.245 (+0.162, +0.329)	+0.026	+0.205	+0.120 (+0.004, +0.227)
Luding (China)	0.32	2,098 / 3,834	0.50 / 0.56	+0.177 (+0.143, +0.214)	+0.273 (+0.207, +0.342)	+0.078	+0.098	+0.096 (+0.034, +0.162)
Chittagong (Bangladesh)	0.38	448 / 896	0.58 / 0.72	+0.213 (+0.139, +0.287)	+0.098 (+0.045, +0.171)	+0.316	+0.132	−0.115 (−0.180, −0.058)
Northern Vietnam	0.41	562 / 1,055	0.48 / 0.67	+0.135 (+0.009, +0.268)	+0.047 (+0.011, +0.079)	+0.204	+0.147	−0.089 (−0.235, +0.044)
Fujian (China)	0.43	91 / 182	0.61 / 0.74	+0.008 (−0.054, +0.073)	+0.001 (−0.043, +0.053)	+0.155	+0.052	−0.007 (−0.091, +0.084)
Luzon (Philippines)	0.43	806 / 1,613	0.58 / 0.68	+0.184 (+0.156, +0.211)	+0.128 (+0.093, +0.168)	+0.209	+0.154	−0.055 (−0.101, −0.004)
Lushan (China)	0.58	437 / 517	0.71 / 0.86	+0.078 (+0.039, +0.123)	+0.047 (+0.024, +0.072)	+0.175	+0.063	−0.031 (−0.085, +0.018)
Agatha (Mexico)	0.59	964 / 733	0.55 / 0.66	+0.036 (−0.050, +0.119)	+0.071 (+0.020, +0.117)	+0.020	+0.142	+0.036 (−0.071, +0.136)
Emilia-Romagna (Italy)	0.63	3,000 / 5,997	0.84 / 0.91	+0.007 (−0.019, +0.035)	−0.005 (−0.015, +0.005)	−0.079	+0.003	−0.012 (−0.041, +0.016)
Freddy (Malawi)	0.81	523 / 862	0.58 / 0.79	+0.187 (+0.103, +0.255)	+0.066 (+0.046, +0.086)	+0.137	+0.087	−0.121 (−0.191, −0.033)
Pasaman, West Sumatra (Indonesia)	0.85	100 / 219	0.55 / 0.84	+0.324 (+0.194, +0.452)	+0.060 (+0.010, +0.116)	+0.361	+0.156	−0.264 (−0.396, −0.128)
São Paulo coast (Brazil)	0.86	82 / 89	0.45 / 0.68	+0.250 (+0.067, +0.414)	+0.119 (+0.047, +0.195)	+0.490	+0.208	−0.131 (−0.284, +0.028)

Table S4. Map-level results for nine events: the share of landslide area within the top 10% of the map domain with the prior-year and event-year inputs, and paired gains (95% CIs). The last column gives the point-AUC increment on the same maps.

Event	f	Model	Top-10% capture Y−1 → Y	Event year	Placebo	Year after	Point AUC increment (same maps)
Mesetas (Colombia)	0.02	LightGBM	0.53 → 0.56	+0.033 (+0.002, +0.057)	+0.039 (+0.010, +0.073)	+0.246	+0.002
	0.02	CNN2D	0.59 → 0.63	+0.045 (+0.014, +0.073)	+0.028 (−0.010, +0.076)	+0.241	+0.014
Jishishan (China)	0.04	LightGBM	0.26 → 0.33	+0.074 (+0.044, +0.102)	+0.011 (−0.006, +0.031)	+0.119	+0.031
	0.04	CNN2D	0.38 → 0.44	+0.052 (+0.019, +0.082)	−0.027 (−0.063, +0.002)	+0.092	+0.022
Palu (Indonesia)	0.26	LightGBM	0.22 → 0.46	+0.248 (+0.177, +0.311)	—	+0.485	+0.113
	0.26	CNN2D	0.25 → 0.54	+0.295 (+0.190, +0.371)	—	+0.425	+0.141
Mangkhut, Itogon (Philippines)	0.29	LightGBM	0.35 → 0.60	+0.254 (+0.218, +0.286)	—	+0.237	+0.047
	0.29	CNN2D	0.29 → 0.53	+0.247 (+0.178, +0.300)	—	+0.206	+0.087
Eastern Iburi (Japan)	0.32	LightGBM	0.10 → 0.48	+0.387 (+0.331, +0.447)	—	+0.469	+0.102
	0.32	CNN2D	0.15 → 0.61	+0.458 (+0.341, +0.581)	—	+0.421	+0.119
Luding (China)	0.32	LightGBM	0.25 → 0.56	+0.315 (+0.259, +0.349)	−0.035 (−0.054, −0.014)	+0.313	+0.085
	0.32	CNN2D	0.35 → 0.68	+0.336 (+0.278, +0.388)	−0.024 (−0.051, +0.006)	+0.278	+0.103
Lushan (China)	0.58	LightGBM	0.45 → 0.71	+0.257 (+0.212, +0.295)	−0.008 (−0.019, +0.011)	+0.239	+0.083
	0.58	CNN2D	0.48 → 0.73	+0.248 (+0.191, +0.306)	+0.013 (−0.014, +0.033)	+0.237	+0.079
Emilia-Romagna (Italy)	0.63	LightGBM	0.51 → 0.67	+0.158 (+0.137, +0.180)	+0.009 (−0.002, +0.019)	+0.133	+0.025
	0.63	CNN2D	0.58 → 0.68	+0.104 (+0.080, +0.127)	+0.005 (−0.012, +0.021)	+0.099	+0.012
Pasaman, West Sumatra (Indonesia)	0.85	LightGBM	0.48 → 0.76	+0.281 (+0.196, +0.350)	+0.052 (+0.016, +0.101)	+0.239	+0.078
	0.85	CNN2D	0.59 → 0.75	+0.161 (+0.089, +0.233)	+0.028 (−0.007, +0.062)	+0.095	+0.064

Table S5. Forward tests as first computed in the initial analyses (Emilia-Romagna and western North Carolina). Table S14 gives the recomputed values used in the main text.

Region	Scenario (training → prediction input)	AUC, all test landslides	AUC, new landslides	AUC, reactivation / expansion	Top-10% capture
Emilia-Romagna	L static factors	0.629	0.569	0.707	0.19
Emilia-Romagna	F1 AE2022 -> AE2022	0.553	0.460	0.676	0.15
Emilia-Romagna	F2 AE2022 -> AE2023 (post-event input)	0.577	0.504	0.674	0.13
Emilia-Romagna	F3 AE2023 -> AE2023 (same-year)	0.558	0.472	0.671	0.12
Emilia-Romagna	L+F1 factors + AE2022	0.568	0.478	0.688	0.14
Western North Carolina	L	0.725	0.713	0.787	0.31
Western North Carolina	F1 AE2023->AE2023	0.762	0.746	0.842	0.42
Western North Carolina	F2 AE2023->AE2024	0.820	0.812	0.859	0.52
Western North Carolina	F3 AE2024->AE2024	0.788	0.776	0.849	0.46
Western North Carolina	L+F1	0.760	0.742	0.847	0.37
Western North Carolina	T1 TESS2023->TESS2023	0.661	0.631	0.807	0.26
Western North Carolina	T2 TESS2023->TESS2024	0.633	0.610	0.744	0.23
Western North Carolina	T3 TESS2024->TESS2024	0.662	0.636	0.793	0.27
Western North Carolina	L+T1	0.739	0.718	0.841	0.33

Table S6. Truncated Sentinel-2 windows within the event year (point LightGBM). AUCs below 0.5 indicate features that do not transfer spatially.

Event	f	Points	Scenes before / after the event	AUC, previous year	AUC, event year before the event	AUC, whole event year	AUC, event year after the event
Nalgae, Mindanao (Philippines)	0.18	163	18 / 4	0.531	0.488	0.479	0.562
Palu (Indonesia)	0.26	991	18 / 6	0.472	0.567	0.617	0.630
Eastern Iburi (Japan)	0.32	5,331	6 / 3	0.425	0.489	0.504	0.659
Luding (China)	0.32	5,638	30 / 15	0.490	0.544	0.570	0.599
Chittagong (Bangladesh)	0.38	1,344	11 / 8	0.540	0.586	0.863	0.828
Northern Vietnam	0.41	1,613	50 / 36	0.496	0.527	0.721	0.810
Fujian (China)	0.43	273	7 / 5	0.606	0.594	0.735	0.766
Luzon (Philippines)	0.43	2,307	42 / 30	0.542	0.570	0.790	0.857
Lushan (China)	0.58	912	10 / 10	0.595	0.626	0.779	0.816
Agatha (Mexico)	0.59	1,695	5 / 7	0.602	0.551	0.622	0.643
Emilia-Romagna (Italy)	0.63	8,849	24 / 47	0.427	0.379	0.357	0.408
Freddy (Malawi)	0.81	507	6 / 18	0.455	0.547	0.593	0.654
Pasaman, West Sumatra (Indonesia)	0.85	256	3 / 16	0.463	0.425	0.744	0.774
São Paulo coast (Brazil)	0.86	171	1 / 11	0.258	0.432	0.769	0.721

Table S7. Re-analysis of the setting of Cheng et al. (2026). **P1:** random 70:30 split; five seeds; t-based CIs. **P2:** spatial 5-fold cross-validation with a 500 m buffer; 30-cluster bootstrap. **P1paper:** the full published protocol. **LCF:** our six terrain factors; the original study used 14.

Protocol	Sample	Model	AUC LCF	AUC AE2022 (pre-event)	AUC AE2023 (event year)	Event year (AE2023 − AE2022)	Placebo (AE2022 − AE2021)	Pre-event vs LCF (AE2022 − LCF)
P1	2,614 + 2,614	CNN1D	0.864	0.918	0.953	+0.034 (+0.027, +0.041)	+0.000 (−0.008, +0.008)	+0.055 (+0.043, +0.067)
P1	2,614 + 2,614	CNN2D	0.895	0.944	0.961	+0.017 (+0.012, +0.022)	−0.001 (−0.009, +0.008)	+0.048 (+0.038, +0.059)
P1	2,614 + 2,614	ViT	0.904	0.947	0.967	+0.020 (+0.012, +0.028)	−0.002 (−0.011, +0.007)	+0.043 (+0.033, +0.053)
P1	2,614 + 2,614	LightGBM	0.860	0.924	0.956	+0.032 (+0.025, +0.038)	+0.000 (−0.003, +0.004)	+0.065 (+0.055, +0.075)
P1	10,365 + 10,365	CNN1D	0.881	0.943	0.970	+0.027 (+0.024, +0.031)	+0.000 (−0.002, +0.002)	+0.061 (+0.056, +0.066)
P1	10,365 + 10,365	CNN2D	0.916	0.969	0.980	+0.011 (+0.008, +0.013)	+0.001 (−0.004, +0.006)	+0.053 (+0.049, +0.057)
P1	10,365 + 10,365	ViT	0.948	0.973	0.986	+0.013 (+0.009, +0.016)	−0.002 (−0.004, +0.001)	+0.025 (+0.021, +0.030)
P1	10,365 + 10,365	LightGBM	0.884	0.942	0.969	+0.027 (+0.024, +0.030)	−0.002 (−0.003, −0.001)	+0.058 (+0.055, +0.061)
P2	2,614 + 2,614	CNN1D	0.792	0.838	0.915	+0.076 (+0.039, +0.117)	−0.006 (−0.018, +0.006)	+0.048 (+0.028, +0.074)
P2	2,614 + 2,614	CNN2D	0.818	0.858	0.902	+0.042 (+0.009, +0.077)	+0.002 (−0.017, +0.021)	+0.040 (+0.015, +0.070)
P2	2,614 + 2,614	ViT	0.809	0.834	0.897	+0.064 (+0.029, +0.107)	−0.010 (−0.028, +0.007)	+0.037 (+0.005, +0.077)
P2	2,614 + 2,614	LightGBM	0.783	0.829	0.913	+0.084 (+0.044, +0.129)	−0.003 (−0.015, +0.009)	+0.046 (+0.015, +0.078)
P2	10,365 + 10,365	CNN1D	0.800	0.857	0.929	+0.069 (+0.035, +0.108)	−0.012 (−0.030, +0.001)	+0.060 (+0.036, +0.089)
P2	10,365 + 10,365	CNN2D	0.830	0.861	0.920	+0.057 (+0.029, +0.089)	+0.003 (−0.010, +0.017)	+0.038 (+0.009, +0.072)
P2	10,365 + 10,365	ViT	0.812	0.851	0.936	+0.086 (+0.046, +0.132)	−0.011 (−0.030, +0.004)	+0.034 (+0.007, +0.063)
P2	10,365 + 10,365	LightGBM	0.808	0.848	0.928	+0.079 (+0.041, +0.121)	−0.009 (−0.022, +0.002)	+0.041 (+0.014, +0.068)
P1paper	2,614 + 2,614	CNN1D	0.868	0.928	0.958	+0.031 (+0.023, +0.038)	—	+0.059 (+0.048, +0.070)
P1paper	2,614 + 2,614	CNN2D	0.910	0.953	0.969	+0.015 (+0.012, +0.019)	—	+0.044 (+0.038, +0.049)
P1paper	2,614 + 2,614	ViT	0.919	0.955	0.972	+0.016 (+0.011, +0.022)	—	+0.037 (+0.031, +0.043)

Table S8. Cross-year stability of the two embedding products at control points. Stability index = $(c_{same} - c_{rand})/(1 - c_{rand})$.

Event (control points)	Years	AlphaEarth cosine, same site	AlphaEarth cosine, random pairs	AlphaEarth stability index	TESSERA cosine, same site	TESSERA cosine, random pairs	TESSERA stability index
Helene, southern Appalachians (USA)	2022→2023	0.982	0.732	0.933	0.914	0.698	0.715
Helene, southern Appalachians (USA)	2023→2024	0.983	0.742	0.935	0.908	0.704	0.689
Emilia-Romagna (Italy)	2021→2022	0.973	0.584	0.936	0.910	0.516	0.814
Jishishan (China)	2021→2022	0.977	0.688	0.925	0.860	0.638	0.613
Lushan (China)	2020→2021	0.979	0.698	0.930	0.873	0.701	0.578
Mesetas (Colombia)	2017→2018	0.965	0.671	0.894	0.840	0.715	0.439
Luding (China)	2020→2021	0.984	0.612	0.958	0.888	0.630	0.698
Fujian (China)	2021→2022	0.950	0.746	0.801	0.851	0.711	0.484

Table S9. Calendar, clear-sky and composite post-event fractions.

Event	Date	f (calendar)	f_clear (clear Sentinel-2 observations)	Clear-sky rate before / after the event	f_comp (observations in the Sentinel-2 composite)
Mesetas (Colombia)	2019-12-24	0.02	0.02	0.12 / 0.08	0.00
Jishishan (China)	2023-12-18	0.04	0.05	0.58 / 0.82	—
Nalgae, Mindanao (Philippines)	2022-10-28	0.18	0.24	0.25 / 0.39	0.23
Helene, southern Appalachians (USA)	2024-09-27	0.26	0.28	0.39 / 0.45	—
Palu (Indonesia)	2018-09-28	0.26	0.18	0.48 / 0.25	0.22
Mangkhut, Itogon (Philippines)	2018-09-15	0.29	0.32	0.37 / 0.44	—
Eastern Iburi (Japan)	2018-09-06	0.32	0.43	0.22 / 0.32	0.30
Luding (China)	2022-09-05	0.32	0.30	0.38 / 0.33	0.29
Chittagong (Bangladesh)	2023-08-16	0.38	0.43	0.50 / 0.62	0.39
Northern Vietnam	2023-08-04	0.41	0.37	0.24 / 0.21	0.45
Fujian (China)	2023-07-28	0.43	0.48	0.32 / 0.40	0.40
Luzon (Philippines)	2023-07-26	0.43	0.32	0.32 / 0.20	0.39
Lushan (China)	2022-06-01	0.58	0.56	0.19 / 0.17	0.47
Agatha (Mexico)	2022-05-30	0.59	0.40	0.88 / 0.42	0.38
Emilia-Romagna (Italy)	2023-05-16	0.63	0.78	0.21 / 0.45	0.72
Freddy (Malawi)	2023-03-12	0.81	0.93	0.18 / 0.55	0.93
Pasaman, West Sumatra (Indonesia)	2022-02-25	0.85	0.90	0.11 / 0.18	0.84
São Paulo coast (Brazil)	2023-02-19	0.86	0.86	0.49 / 0.47	0.91

Table S10. All prespecified criteria and their outcomes, in the order in which they were specified (including the follow-up analyses).

Specified (UTC, 2026)	Analysis	Criterion	Outcome
4 Oct 14:08	Transition-zone prediction	≥ 2 of 3 added events with $d_0/d_1 < 0.8$	**Met**: Iburi 0.64, Luding 0.60 when first evaluated on the earlier point sample; 0.65 and 0.61 in the final audit (Nalgae excluded by the prior rule)
8 Oct 13:35	Audit, patch CNN2D (16 events)	pooled $d_0 > 0$, ≥ 12/16 positive, placebo TOST ±0.01	**Met**: +0.069 (0.043–0.095), 14/16; TOST $p < 0.001$
8 Oct 16:15	Sentinel-2 composites leak (patch)	pooled $d_0 > 0$	**Met**: +0.126
8 Oct 16:15	AlphaEarth vs Sentinel-2 (patch)	CI of the difference: contains 0 / > 0 / < 0	**< 0**: −0.045 (−0.085 to −0.005); Sentinel-2 pre-event AUC ≈ 0.55
8 Oct 16:15	Composite-subset placebo	TOST ±0.01	**Not met**
10 Oct ≈10:32	Dose–response without a visibility rule	linear slope > 0, $p < 0.05$, both models	**Met** (16 events: $p = 0.0001$, 0.0009; 18 events: 0.0003, 0.0005)
10 Oct ≈10:32	Earthquakes only	slope > 0, $p < 0.05$	**Met**: $p < 0.0001$
10 Oct ≈10:32	Emilia-Romagna whole-region map	capture gain > 0; placebo TOST ±0.02	**Met**: +0.158, +0.104; TOST $p = 0.021$, 0.038
10 Oct (hash)	Autumn rainfall P1	Helene and Mangkhut $d_0/d_1 < 0.90$	**Not met**: Helene 0.59/0.50; Mangkhut 0.96/1.50 as evaluated (bootstrap medians), 0.97/1.52 as ratios of the full-sample increments
10 Oct (hash)	Autumn rainfall P2	rainfall-only slope $p < 0.05$, both models	**Not met**: point 0.040; patch 0.16
10 Oct (hash)	Autumn rainfall P3	f_{50} within the earlier interval	**Met**: 0.24, 0.26
14 Oct 10:31	Map gain, $f \geq 0.35$ with visible signal	pooled gain > 0, both models	**Formally met** ($k = 2$ and 1)
14 Oct 10:31	Map placebo	TOST ±0.02	**Not met**: $p = 0.17$, 0.063
14 Oct 16:07	TESSERA leaks	pooled $d_0 > 0$ ($f \geq 0.35$, visible)	**Met**: +0.134 (0.090–0.179)
14 Oct 16:07	TESSERA placebo	TOST ±0.01	**Not met**: $p = 0.15$
14 Oct 16:07	TESSERA dose–response	slope $p < 0.05$	**Met**: $p = 0.00002$
14 Oct 16:07	Clear-sky dose	f_{clear} improves log-likelihood by ≥ 1, both models	**Rejected**: worse by 2.68 and 1.87
14 Oct 16:07	Clear-sky explains Mangkhut	$f_{\text{clear}} - f \geq 0.10$	**Not met**: +0.03
14 Oct 16:07	Inventory timing (unadjusted NDVI)	method check	**Method failed**; discarded
14 Oct 17:14	Recovery weakens the year-after reference (NDVI)	Spearman > 0, $p < 0.05$	**Formally met** (0.74, $p = 0.018$), confounded by f
15 Oct 00:09	Inventory timing (phenology-corrected)	check ≤ 10%; predicted Mangkhut ratio ≥ 0.90	**Check met** (9.6%); **prediction not met** (0.87, 0.70)
15 Oct 00:49	Composite-weighted dose	log-likelihood improves by ≥ 1	**Not met**
15 Oct 00:54	North Carolina forward value	sign of F1 − L	**F1 > L**: +0.037
15 Oct 00:54	North Carolina forward leakage	F2 − F1 > 0	**Met**: +0.058
16 Oct ≈03:23	Recovery (a)	decay ratio $q \geq 0.90$	**Not met**: $q = 0.77$, 0.76
16 Oct ≈03:23	Recovery (b)	adjusted slope $p < 0.05$ and f_{50} in 0.15–0.45	**Met**: $p = 0.004$, 0.002; $f_{50} = 0.23$, 0.26
16 Oct ≈03:23	Recovery (c)	adjusted plateau compatible with 1	**Met**: 0.96, 0.99 (0.87–1.08)
16 Oct ≈03:23	Fixed 12-month reference (Sentinel-2)	slope $p < 0.05$	**Met**: $p = 0.0006$ (point), 0.011 (patch)
16 Oct ≈03:23	Training × prediction decomposition	interpretation rules for the two components	prediction-time component ≈ 0 (CI includes 0); training component < 0, both models
16 Oct ≈03:23	Placebo-corrected increment	pooled > 0, CI excludes 0, both models	**Met**: +0.085, +0.064
16 Oct ≈03:23	REML–HKSJ re-pooling	conclusions unchanged	**Met**
16 Oct ≈03:23	Forward temporal independence	signs and significance of F1 − L and F2 − F1 unchanged	**Met**
16 Oct ≈03:23	Forward spatial independence	F2 − F1 > 0 at all distances; F1 − L sign kept	F2 − F1 > 0 at all distances (CI includes 0 only in Emilia-Romagna > 500 m); F1 − L not significant in North Carolina > 500 m
16 Oct ≈03:23	Scar direction	projection AUC > 0.5 in both regions, North Carolina > Emilia-Romagna	**Met**: 0.645, 0.595
16 Oct ≈03:23	Mangkhut and mining	both ratios < 0.90 after exclusion	**Not met**: point 0.85–0.89, patch 1.26–1.48

Specified (UTC, 2026)	Analysis	Criterion	Outcome
16 Oct ≈03:23	Lushan forward test	F1 − L > 0 (label-match prediction); F2 − F1 > 0	F1 − L **undecided** (+0.024, −0.025 to 0.071, with the prespecified static factors; +0.031, −0.019 to 0.080, in the first run without log upslope area); F2 − F1 **met** (+0.113)

Table S11. Training-year × prediction-year decomposition per event (AlphaEarth). AUC *a*→*b* is the out-of-fold AUC of models trained with year *a* inputs and applied with year *b* inputs. Components are relative to the clean model (Y−1→Y−1), with 95% cluster-bootstrap CIs.

Event	f	Model	AUC Y−1→Y−1	AUC Y−1→Y	AUC Y→Y−1	AUC Y→Y	Prediction-time component	Training component	Event-year increment
Mesetas (Colombia)	0.02	LightGBM	0.855	0.848	0.834	0.861	−0.007 (−0.017, +0.002)	−0.021 (−0.037, −0.003)	+0.006 (−0.006, +0.019)
	0.02	CNN2D	0.878	0.870	0.865	0.897	−0.007 (−0.022, +0.010)	−0.013 (−0.025, +0.000)	+0.019 (+0.007, +0.032)
Jishishan (China)	0.04	LightGBM	0.591	0.568	0.542	0.617	−0.023 (−0.048, +0.010)	−0.048 (−0.062, −0.034)	+0.026 (+0.004, +0.048)
	0.04	CNN2D	0.734	0.656	0.671	0.717	−0.078 (−0.131, −0.014)	−0.063 (−0.130, −0.008)	−0.017 (−0.056, +0.016)
Nalgae, Mindanao (Philippines)	0.18	LightGBM	0.804	0.801	0.770	0.839	−0.003 (−0.027, +0.018)	−0.034 (−0.061, −0.003)	+0.036 (+0.016, +0.064)
	0.18	CNN2D	0.768	0.754	0.761	0.753	−0.013 (−0.034, +0.007)	−0.006 (−0.029, +0.018)	−0.015 (−0.044, +0.015)
Helene, southern Appalachians (USA)	0.26	LightGBM	0.815	0.849	0.795	0.888	+0.034 (+0.026, +0.043)	−0.020 (−0.031, −0.010)	+0.073 (+0.064, +0.084)
	0.26	CNN2D	0.801	0.799	0.760	0.866	−0.002 (−0.017, +0.010)	−0.041 (−0.064, −0.011)	+0.065 (+0.055, +0.078)
Palu (Indonesia)	0.26	LightGBM	0.720	0.705	0.695	0.835	−0.015 (−0.050, +0.018)	−0.025 (−0.054, +0.007)	+0.115 (+0.081, +0.154)
	0.26	CNN2D	0.737	0.768	0.745	0.867	+0.031 (−0.004, +0.078)	+0.009 (−0.028, +0.046)	+0.131 (+0.085, +0.177)
Mangkhut, Itogon (Philippines)	0.29	LightGBM	0.818	0.832	0.745	0.873	+0.014 (+0.002, +0.026)	−0.073 (−0.103, −0.045)	+0.055 (+0.039, +0.069)
	0.29	CNN2D	0.763	0.835	0.728	0.870	+0.072 (+0.024, +0.119)	−0.035 (−0.089, +0.017)	+0.107 (+0.057, +0.159)
Eastern Iburi (Japan)	0.32	LightGBM	0.829	0.761	0.702	0.926	−0.068 (−0.110, −0.030)	−0.127 (−0.176, −0.076)	+0.098 (+0.075, +0.122)
	0.32	CNN2D	0.830	0.726	0.587	0.948	−0.104 (−0.159, −0.054)	−0.243 (−0.304, −0.175)	+0.118 (+0.078, +0.156)
Luding (China)	0.32	LightGBM	0.757	0.760	0.720	0.842	+0.003 (−0.010, +0.017)	−0.037 (−0.062, −0.008)	+0.085 (+0.066, +0.100)
	0.32	CNN2D	0.796	0.798	0.656	0.903	+0.001 (−0.048, +0.033)	−0.140 (−0.194, −0.067)	+0.107 (+0.085, +0.128)
Chittagong (Bangladesh)	0.38	LightGBM	0.808	0.831	0.768	0.936	+0.023 (+0.015, +0.031)	−0.040 (−0.067, −0.013)	+0.128 (+0.106, +0.148)
	0.38	CNN2D	0.804	0.832	0.737	0.894	+0.028 (+0.015, +0.037)	−0.067 (−0.092, −0.040)	+0.090 (+0.070, +0.110)
Northern Vietnam	0.41	LightGBM	0.678	0.702	0.612	0.820	+0.023 (−0.001, +0.051)	−0.067 (−0.098, −0.032)	+0.141 (+0.108, +0.173)
	0.41	CNN2D	0.721	0.727	0.662	0.807	+0.007 (−0.019, +0.028)	−0.059 (−0.095, −0.027)	+0.086 (+0.045, +0.120)
Fujian (China)	0.43	LightGBM	0.822	0.801	0.789	0.890	−0.020 (−0.040, +0.001)	−0.032 (−0.061, +0.002)	+0.069 (+0.050, +0.094)
	0.43	CNN2D	0.800	0.794	0.761	0.825	−0.006 (−0.030, +0.020)	−0.039 (−0.062, −0.006)	+0.025 (−0.005, +0.053)
Luzon (Philippines)	0.43	LightGBM	0.727	0.750	0.687	0.927	+0.023 (+0.004, +0.041)	−0.040 (−0.056, −0.019)	+0.200 (+0.178, +0.224)
	0.43	CNN2D	0.729	0.740	0.656	0.931	+0.011 (−0.009, +0.031)	−0.073 (−0.100, −0.045)	+0.202 (+0.179, +0.230)
Lushan (China)	0.58	LightGBM	0.833	0.869	0.823	0.924	+0.035 (+0.016, +0.057)	−0.010 (−0.028, +0.006)	+0.091 (+0.071, +0.115)
	0.58	CNN2D	0.842	0.860	0.849	0.921	+0.018 (+0.004, +0.034)	+0.006 (−0.005, +0.017)	+0.079 (+0.056, +0.106)
Agatha (Mexico)	0.59	LightGBM	0.766	0.738	0.667	0.910	−0.028 (−0.045, −0.010)	−0.100 (−0.129, −0.072)	+0.144 (+0.116, +0.172)
	0.59	CNN2D	0.789	0.721	0.676	0.882	−0.068 (−0.104, −0.027)	−0.113 (−0.161, −0.068)	+0.093 (+0.066, +0.119)
Emilia-Romagna (Italy)	0.63	LightGBM	0.908	0.888	0.844	0.933	−0.020 (−0.026, −0.014)	−0.064 (−0.078, −0.053)	+0.025 (+0.019, +0.031)
	0.63	CNN2D	0.935	0.837	0.870	0.951	−0.098 (−0.118, −0.078)	−0.065 (−0.081, −0.052)	+0.015 (+0.011, +0.021)
Freddy (Malawi)	0.81	LightGBM	0.853	0.846	0.838	0.912	−0.007 (−0.018, +0.005)	−0.016 (−0.030, −0.002)	+0.058 (+0.038, +0.079)
	0.81	CNN2D	0.833	0.826	0.810	0.871	−0.008 (−0.020, +0.008)	−0.023 (−0.044, −0.004)	+0.038 (+0.015, +0.064)
Pasaman, West Sumatra (Indonesia)	0.85	LightGBM	0.884	0.936	0.863	0.974	+0.052 (+0.033, +0.072)	−0.021 (−0.043, −0.001)	+0.090 (+0.058, +0.124)
	0.85	CNN2D	0.907	0.932	0.839	0.960	+0.025 (+0.011, +0.043)	−0.068 (−0.123, −0.013)	+0.053 (+0.030, +0.082)
São Paulo coast (Brazil)	0.86	LightGBM	0.791	0.748	0.724	0.957	−0.042 (−0.069, −0.011)	−0.066 (−0.118, −0.005)	+0.167 (+0.113, +0.228)
	0.86	CNN2D	0.798	0.761	0.760	0.885	−0.037 (−0.060, −0.013)	−0.038 (−0.085, +0.020)	+0.088 (+0.045, +0.141)

Event	f	Model	AUC Y−1→Y−1	AUC Y−1→Y	AUC Y→Y−1	AUC Y→Y	Prediction-time component	Training component	Event-year increment

Table S12. Increments for the year after next (Y+2; 17 events; Helene has no 2026 product). The decay ratio d_2/d_1 is per event; the pooled decay uses events with a visible year-after signal (Text S1).

Event	f	Model	Event year d0	Year after d1	Year after next d2	d2/d1	Year-after signal visible
Mesetas (Colombia)	0.02	CNN2D	+0.020	+0.081	+0.053	0.65	yes
Mesetas (Colombia)	0.02	LightGBM	+0.006	+0.090	+0.062	0.69	yes
Jishishan (China)	0.04	CNN2D	−0.017	+0.040	+0.073	1.84	yes
Jishishan (China)	0.04	LightGBM	+0.026	+0.026	+0.021	0.80	yes
Nalgae, Mindanao (Philippines)	0.18	CNN2D	−0.015	−0.024	−0.007	0.29	no
Nalgae, Mindanao (Philippines)	0.18	LightGBM	+0.036	+0.017	+0.042	2.53	no
Palu (Indonesia)	0.26	CNN2D	+0.131	+0.209	+0.205	0.98	yes
Palu (Indonesia)	0.26	LightGBM	+0.115	+0.256	+0.242	0.95	yes
Mangkhut, Itogon (Philippines)	0.29	CNN2D	+0.107	+0.071	+0.013	0.19	yes
Mangkhut, Itogon (Philippines)	0.29	LightGBM	+0.055	+0.057	+0.001	0.02	yes
Eastern Iburi (Japan)	0.32	CNN2D	+0.118	+0.152	+0.152	1.00	yes
Eastern Iburi (Japan)	0.32	LightGBM	+0.098	+0.152	+0.150	0.99	yes
Luding (China)	0.32	CNN2D	+0.107	+0.134	+0.118	0.88	yes
Luding (China)	0.32	LightGBM	+0.085	+0.139	+0.126	0.91	yes
Chittagong (Bangladesh)	0.38	CNN2D	+0.090	+0.061	+0.022	0.37	yes
Chittagong (Bangladesh)	0.38	LightGBM	+0.128	+0.105	+0.069	0.65	yes
Northern Vietnam	0.41	CNN2D	+0.086	+0.075	+0.021	0.27	yes
Northern Vietnam	0.41	LightGBM	+0.141	+0.145	+0.081	0.56	yes
Fujian (China)	0.43	CNN2D	+0.025	+0.016	+0.013	0.80	no
Fujian (China)	0.43	LightGBM	+0.069	+0.075	+0.046	0.61	yes
Luzon (Philippines)	0.43	CNN2D	+0.202	+0.209	+0.162	0.77	yes
Luzon (Philippines)	0.43	LightGBM	+0.200	+0.219	+0.175	0.80	yes
Lushan (China)	0.58	CNN2D	+0.079	+0.080	+0.064	0.80	yes
Lushan (China)	0.58	LightGBM	+0.091	+0.090	+0.073	0.81	yes
Agatha (Mexico)	0.59	CNN2D	+0.093	+0.054	+0.025	0.47	yes
Agatha (Mexico)	0.59	LightGBM	+0.144	+0.114	+0.070	0.61	yes
Emilia-Romagna (Italy)	0.63	CNN2D	+0.015	+0.017	+0.012	0.71	yes
Emilia-Romagna (Italy)	0.63	LightGBM	+0.025	+0.024	+0.015	0.64	yes
Freddy (Malawi)	0.81	CNN2D	+0.038	+0.028	+0.017	0.60	yes
Freddy (Malawi)	0.81	LightGBM	+0.058	+0.044	+0.024	0.55	yes
Pasaman, West Sumatra (Indonesia)	0.85	CNN2D	+0.053	+0.037	+0.018	0.49	yes
Pasaman, West Sumatra (Indonesia)	0.85	LightGBM	+0.090	+0.076	+0.064	0.84	yes
São Paulo coast (Brazil)	0.86	CNN2D	+0.088	+0.064	+0.045	0.70	yes
São Paulo coast (Brazil)	0.86	LightGBM	+0.167	+0.155	+0.140	0.91	yes

Table S13. Sentinel-2 composites with event-relative windows (15 events): increments relative to the prior calendar year for the event year, the calendar year after, the 12 months after the event day, and the 12 months before it. Models: patch CNN2D (11 × 11 cells of 30 m) and LightGBM on the nine channels of the central 30 m cell of each patch ("centre-cell LightGBM"); the latter differs from the 10 m point LightGBM of Table 2.

Event	f	Model	Pre-event AUC (Y−1)	Event year d0	Calendar year after d1	12 months after the event d_fix	12 months before the event
Mesetas (Colombia)	0.02	patch CNN2D	0.451	+0.090	+0.268	+0.292	+0.115
Mesetas (Colombia)	0.02	centre-cell LightGBM	0.516	−0.033	+0.274	+0.274	+0.009
Nalgae, Mindanao (Philippines)	0.18	patch CNN2D	0.566	−0.056	+0.007	+0.046	−0.312
Nalgae, Mindanao (Philippines)	0.18	centre-cell LightGBM	0.461	−0.121	+0.124	+0.213	−0.167
Palu (Indonesia)	0.26	patch CNN2D	0.407	+0.240	+0.516	+0.426	+0.163
Palu (Indonesia)	0.26	centre-cell LightGBM	0.466	+0.170	+0.465	+0.385	+0.129
Eastern Iburi (Japan)	0.32	patch CNN2D	0.475	+0.125	+0.460	+0.448	−0.140
Eastern Iburi (Japan)	0.32	centre-cell LightGBM	0.389	+0.024	+0.394	+0.387	−0.065
Luding (China)	0.32	patch CNN2D	0.500	+0.179	+0.290	+0.301	+0.062
Luding (China)	0.32	centre-cell LightGBM	0.511	+0.089	+0.217	+0.215	+0.036
Chittagong (Bangladesh)	0.38	patch CNN2D	0.576	+0.215	+0.044	+0.223	+0.032
Chittagong (Bangladesh)	0.38	centre-cell LightGBM	0.553	+0.336	+0.108	+0.284	−0.011
Northern Vietnam	0.41	patch CNN2D	0.477	+0.143	+0.151	+0.259	+0.086
Northern Vietnam	0.41	centre-cell LightGBM	0.497	+0.189	+0.206	+0.299	+0.014
Fujian (China)	0.43	patch CNN2D	0.606	+0.010	+0.038	+0.056	−0.038
Fujian (China)	0.43	centre-cell LightGBM	0.573	+0.100	+0.249	+0.226	−0.013
Luzon (Philippines)	0.43	patch CNN2D	0.578	+0.184	+0.292	+0.320	−0.000
Luzon (Philippines)	0.43	centre-cell LightGBM	0.516	+0.269	+0.382	+0.407	+0.020
Lushan (China)	0.58	patch CNN2D	0.706	+0.076	+0.157	+0.097	−0.008
Lushan (China)	0.58	centre-cell LightGBM	0.645	+0.172	+0.171	+0.185	−0.023
Agatha (Mexico)	0.59	patch CNN2D	0.554	+0.036	+0.051	+0.100	+0.048
Agatha (Mexico)	0.59	centre-cell LightGBM	0.552	+0.096	+0.147	+0.071	+0.017
Emilia-Romagna (Italy)	0.63	patch CNN2D	0.842	+0.006	+0.012	−0.054	−0.026
Emilia-Romagna (Italy)	0.63	centre-cell LightGBM	0.746	−0.042	+0.028	−0.037	+0.024
Freddy (Malawi)	0.81	patch CNN2D	0.575	+0.191	+0.195	+0.196	−0.012
Freddy (Malawi)	0.81	centre-cell LightGBM	0.573	+0.179	+0.148	+0.193	−0.006
Pasaman, West Sumatra (Indonesia)	0.85	patch CNN2D	0.549	+0.325	+0.071	+0.385	−0.010
Pasaman, West Sumatra (Indonesia)	0.85	centre-cell LightGBM	0.395	+0.414	+0.088	+0.447	+0.027
São Paulo coast (Brazil)	0.86	patch CNN2D	0.451	+0.255	+0.151	+0.226	−0.001
São Paulo coast (Brazil)	0.86	centre-cell LightGBM	0.281	+0.523	+0.440	+0.535	+0.053

Table S14. Forward tests in three regions: main analyses and robustness to temporal and spatial independence (95% cluster-bootstrap CIs). Distance subsets keep only test landslides and test controls beyond the given distance from the historical inventory. Lushan rows use the prespecified static factors including log upslope area; the last row gives the first run without it (not as prespecified; Text S3, item 15).

Region	Training set / test subset	Landslides + controls (test)	AUC L	AUC F1	AUC F2	AUC F3	AUC F4	F1 – L	F2 – F1	F3 – F1	F4 – F1
W North Carolina	main	2,025 + 3,685	0.725	0.762	0.820	0.788	0.748	+0.037 (+0.019, +0.057)	+0.058 (+0.043, +0.071)	+0.026 (+0.017, +0.035)	−0.014 (−0.027, −0.001)

Region	Training set / test subset	Landslides + controls (test)	AUC L	AUC F1	AUC F2	AUC F3	AUC F4	F1 – L	F2 – F1	F3 – F1	F4 – F1
W North Carolina	main; test landslides and controls > 50 m from USLI	1,683 + 3,359	0.719	0.756	0.817	0.784	0.736	+0.037 (+0.016, +0.061)	+0.061 (+0.045, +0.075)	+0.028 (+0.018, +0.039)	−0.020 (−0.035, −0.005)
W North Carolina	main; test landslides and controls > 100 m from USLI	1,512 + 3,174	0.719	0.752	0.815	0.781	0.733	+0.034 (+0.012, +0.057)	+0.062 (+0.047, +0.076)	+0.029 (+0.019, +0.041)	−0.020 (−0.036, −0.004)
W North Carolina	main; test landslides and controls > 250 m from USLI	1,147 + 2,720	0.713	0.741	0.808	0.770	0.719	+0.028 (+0.004, +0.053)	+0.067 (+0.050, +0.084)	+0.030 (+0.017, +0.044)	−0.022 (−0.040, −0.003)
W North Carolina	main; test landslides and controls > 500 m from USLI	854 + 2,238	0.713	0.729	0.802	0.759	0.704	+0.016 (−0.013, +0.043)	+0.073 (+0.052, +0.093)	+0.030 (+0.012, +0.046)	−0.025 (−0.047, −0.005)
W North Carolina	dated (< 2024) training landslides only	2,025 + 3,685	0.750	0.791	0.843	0.815	0.784	+0.041 (+0.021, +0.061)	+0.052 (+0.041, +0.063)	+0.024 (+0.016, +0.033)	−0.007 (−0.021, +0.007)
W North Carolina	training landslides > 100 m from every Helene point	2,025 + 3,685	0.718	0.762	0.820	0.783	0.749	+0.044 (+0.025, +0.065)	+0.058 (+0.043, +0.071)	+0.020 (+0.011, +0.030)	−0.014 (−0.027, −0.000)
W North Carolina	dated ≤ 2010 only	2,025 + 3,685	0.730	0.780	0.839	0.800	0.757	+0.050 (+0.027, +0.072)	+0.060 (+0.047, +0.073)	+0.020 (+0.012, +0.029)	−0.023 (−0.039, −0.005)
W North Carolina	dated ≥ 2011 only	2,025 + 3,685	0.711	0.769	0.798	0.799	0.768	+0.058 (+0.038, +0.079)	+0.030 (+0.020, +0.039)	+0.031 (+0.022, +0.040)	−0.001 (−0.009, +0.007)
Emilia-Romagna	main	20,000 + 40,000	0.629	0.553	0.577	0.558	0.587	−0.076 (−0.093, −0.057)	+0.024 (+0.008, +0.039)	+0.005 (−0.003, +0.012)	+0.034 (+0.021, +0.046)
Emilia-Romagna	main; test landslides and controls > 50 m from IFFI	11,360 + 21,301	0.654	0.566	0.601	0.582	0.604	−0.088 (−0.107, −0.067)	+0.035 (+0.018, +0.051)	+0.016 (+0.008, +0.023)	+0.038 (+0.025, +0.052)
Emilia-Romagna	main; test landslides and controls > 100 m from IFFI	7,788 + 15,456	0.674	0.583	0.621	0.602	0.623	−0.091 (−0.114, −0.068)	+0.037 (+0.019, +0.054)	+0.019 (+0.010, +0.027)	+0.039 (+0.025, +0.054)
Emilia-Romagna	main; test landslides and controls > 250 m from IFFI	3,368 + 7,586	0.710	0.620	0.656	0.636	0.655	−0.090 (−0.118, −0.062)	+0.036 (+0.014, +0.054)	+0.016 (+0.003, +0.027)	+0.035 (+0.017, +0.053)
Emilia-Romagna	main; test landslides and controls > 500 m from IFFI	924 + 2,841	0.711	0.631	0.660	0.643	0.664	−0.081 (−0.116, −0.043)	+0.029 (−0.007, +0.055)	+0.012 (−0.010, +0.029)	+0.033 (+0.008, +0.052)
Emilia-Romagna	training IFFI crowns > 100 m from 2023 landslides	20,000 + 40,000	0.544	0.469	0.496	0.441	0.530	−0.075 (−0.095, −0.055)	+0.027 (+0.008, +0.043)	−0.028 (−0.036, −0.020)	+0.061 (+0.046, +0.074)
Emilia-Romagna	training IFFI crowns > 250 m from 2023 landslides	20,000 + 40,000	0.481	0.398	0.446	0.367	0.501	−0.083 (−0.105, −0.060)	+0.049 (+0.030, +0.066)	−0.031 (−0.039, −0.022)	+0.103 (+0.087, +0.118)
Lushan	all test points	1,286 + 2,572	0.574	0.598	0.711	0.730	0.625	+0.024 (−0.025, +0.071)	+0.113 (+0.092, +0.133)	+0.132 (+0.101, +0.164)	+0.028 (+0.007, +0.048)
Lushan	test landslides ≤ 100 m from a 2013 landslide (+ all controls)	608 + 2,572	0.591	0.659	0.748	0.770	0.690	+0.069 (+0.013, +0.114)	+0.089 (+0.070, +0.108)	+0.110 (+0.080, +0.144)	+0.031 (+0.003, +0.057)
Lushan	test landslides > 100 m from a 2013 landslide (+ all controls)	678 + 2,572	0.559	0.542	0.677	0.694	0.567	−0.016 (−0.071, +0.040)	+0.135 (+0.113, +0.156)	+0.151 (+0.117, +0.182)	+0.025 (+0.000, +0.048)
Lushan	test landslides and controls > 100 m from 2013 landslides	678 + 2,253	0.574	0.566	0.700	0.717	0.588	−0.008 (−0.064, +0.050)	+0.134 (+0.112, +0.155)	+0.151 (+0.117, +0.182)	+0.023 (−0.003, +0.046)
Lushan	test landslides and controls > 250 m from 2013 landslides	326 + 1,482	0.591	0.598	0.727	0.744	0.614	+0.008 (−0.076, +0.096)	+0.128 (+0.106, +0.149)	+0.146 (+0.103, +0.183)	+0.016 (−0.014, +0.044)
Lushan	test landslides and controls > 500 m from 2013 landslides	155 + 740	0.629	0.667	0.784	0.794	0.659	+0.038 (−0.067, +0.112)	+0.117 (+0.073, +0.153)	+0.127 (+0.075, +0.175)	−0.008 (−0.039, +0.019)

Lushan	all test points; static factors without log upslope area (first run, not as prespecified)	1,286 + 2,572	0.567	0.598	0.711	0.730	0.625	+0.031 (−0.019, +0.080)	+0.113 (+0.092, +0.133)	+0.132 (+0.101, +0.164)	+0.028 (+0.007, +0.048)

Table S15. Typhoon Mangkhut: event-year and year-after increments after excluding points near mapped mining areas.

Points kept	Model	Points (landslides)	Event year d0	Year after d1	Ratio d0/d1 (95% range)
all	LightGBM	3,300 (1,100)	+0.055 (+0.039, +0.069)	+0.057 (+0.041, +0.072)	0.97 (0.82–1.12)
all	CNN2D	3,300 (1,100)	+0.107 (+0.057, +0.159)	+0.071 (+0.035, +0.103)	1.52 (1.27–1.86)
> 500 m from mapped mining areas	LightGBM	3,227 (1,058)	+0.056 (+0.036, +0.072)	+0.065 (+0.045, +0.085)	0.85 (0.70–1.00)
> 500 m from mapped mining areas	CNN2D	3,227 (1,058)	+0.092 (+0.047, +0.141)	+0.073 (+0.036, +0.110)	1.26 (1.00–1.58)
> 1000 m from mapped mining areas	LightGBM	3,071 (984)	+0.052 (+0.033, +0.070)	+0.059 (+0.038, +0.079)	0.89 (0.73–1.09)
> 1000 m from mapped mining areas	CNN2D	3,071 (984)	+0.094 (+0.053, +0.138)	+0.064 (+0.028, +0.093)	1.48 (1.20–2.09)

Table S16. All pooled results with DerSimonian–Laird and REML–Hartung–Knapp–Sidik–Jonkman pooling, including the placebo-corrected increments (d_0 − placebo). Per-event estimates are bootstrap means; they differ from the full-sample estimates by at most 0.002 (mean 0.0008).

Point set	Representation / model	Contrast	k	DerSimonian–Laird (95% CI)	REML with HKSJ interval	Positive events	TOST p (DL / HKSJ)
AlphaEarth, audit points	LightGBM	event year d_0	18	+0.087 (+0.065, +0.110)	+0.088 (+0.062, +0.114)	18/18	—
AlphaEarth, audit points	LightGBM	placebo	15	+0.002 (−0.003, +0.007)	+0.002 (−0.005, +0.009)	9/15	0.001 / 0.011
AlphaEarth, audit points	LightGBM	year after d_1	18	+0.104 (+0.076, +0.133)	+0.105 (+0.072, +0.137)	18/18	—
AlphaEarth, audit points	LightGBM	d_0 − placebo	15	+0.085 (+0.057, +0.113)	+0.085 (+0.051, +0.120)	14/15	—
AlphaEarth, audit points	CNN2D	event year d_0	18	+0.070 (+0.048, +0.093)	+0.071 (+0.043, +0.098)	16/18	—
AlphaEarth, audit points	CNN2D	placebo	15	−0.002 (−0.006, +0.003)	−0.002 (−0.007, +0.003)	6/15	0.000 / 0.002
AlphaEarth, audit points	CNN2D	year after d_1	18	+0.078 (+0.052, +0.104)	+0.078 (+0.047, +0.110)	17/18	—
AlphaEarth, audit points	CNN2D	d_0 − placebo	15	+0.064 (+0.035, +0.093)	+0.064 (+0.031, +0.096)	14/15	—
TESSERA points	TESSERA	event year d_0	10	+0.104 (+0.073, +0.135)	+0.105 (+0.061, +0.149)	10/10	—
TESSERA points	TESSERA	placebo	10	+0.003 (−0.010, +0.016)	+0.003 (−0.015, +0.020)	5/10	0.148 / 0.184
TESSERA points	TESSERA	year after d_1	10	+0.121 (+0.089, +0.154)	+0.121 (+0.091, +0.151)	10/10	—
TESSERA points	TESSERA	d_0 − placebo	10	+0.103 (+0.058, +0.147)	+0.104 (+0.044, +0.163)	9/10	—
TESSERA points	AlphaEarth	event year d_0	10	+0.071 (+0.047, +0.094)	+0.073 (+0.036, +0.109)	10/10	—
TESSERA points	AlphaEarth	placebo	10	−0.002 (−0.010, +0.006)	−0.003 (−0.014, +0.009)	4/10	0.030 / 0.089
TESSERA points	AlphaEarth	year after d_1	10	+0.088 (+0.055, +0.121)	+0.088 (+0.052, +0.123)	10/10	—
TESSERA points	AlphaEarth	d_0 − placebo	10	+0.072 (+0.044, +0.101)	+0.075 (+0.028, +0.122)	9/10	—
composite subset points	S2 patch CNN2D	d_0 − placebo	13	+0.138 (+0.075, +0.202)	+0.138 (+0.080, +0.195)	13/13	—
composite subset points	AlphaEarth patch CNN2D	d_0 − placebo	13	+0.072 (+0.029, +0.114)	+0.077 (+0.008, +0.145)	10/13	—
composite subset points	S2 point LightGBM	d_0 − placebo	13	+0.159 (+0.074, +0.245)	+0.161 (+0.046, +0.276)	9/13	—
composite subset points	AlphaEarth point LightGBM	d_0 − placebo	13	+0.093 (+0.049, +0.137)	+0.093 (+0.046, +0.139)	11/13	—
composite subset points	S2 patch CNN2D	event year d_0	15	+0.126 (+0.076, +0.175)	+0.126 (+0.069, +0.182)	14/15	—
composite subset points	S2 patch CNN2D	placebo	13	−0.015 (−0.037, +0.007)	−0.015 (−0.044, +0.013)	3/13	0.683 / 0.651
composite subset points	S2 patch CNN2D	year after d_1	15	+0.179 (+0.100, +0.258)	+0.179 (+0.092, +0.266)	15/15	—
composite subset points	AlphaEarth patch CNN2D	event year d_0	15	+0.073 (+0.042, +0.103)	+0.077 (+0.029, +0.124)	12/15	—
composite subset points	AlphaEarth patch CNN2D	placebo	13	−0.009 (−0.024, +0.005)	−0.012 (−0.036, +0.012)	5/13	0.468 / 0.571

Point set	Representation / model	Contrast	k	DerSimonian–Laird (95% CI)	REML with HKSJ interval	Positive events	TOST p (DL / HKSJ)
composite subset points	AlphaEarth patch CNN2D	year after d_1	15	+0.083 (+0.049, +0.116)	+0.090 (+0.030, +0.150)	12/15	—
composite subset points	S2 point LightGBM	event year d_0	15	+0.137 (+0.066, +0.207)	+0.137 (+0.050, +0.225)	12/15	—
composite subset points	S2 point LightGBM	placebo	13	−0.014 (−0.035, +0.008)	−0.014 (−0.038, +0.010)	5/13	0.632 / 0.631
composite subset points	S2 point LightGBM	year after d_1	15	+0.188 (+0.125, +0.252)	+0.187 (+0.126, +0.247)	15/15	—
composite subset points	AlphaEarth point LightGBM	event year d_0	15	+0.098 (+0.060, +0.137)	+0.098 (+0.058, +0.137)	14/15	—
composite subset points	AlphaEarth point LightGBM	placebo	13	−0.005 (−0.020, +0.009)	−0.005 (−0.021, +0.011)	4/13	0.254 / 0.263
composite subset points	AlphaEarth point LightGBM	year after d_1	15	+0.126 (+0.083, +0.169)	+0.127 (+0.071, +0.183)	14/15	—
maps, 9 events (top-10% capture)	LightGBM	event year d_0	9	+0.221 (+0.148, +0.294)	+0.221 (+0.133, +0.309)	9/9	—
maps, 9 events (top-10% capture)	LightGBM	placebo	6	+0.007 (−0.012, +0.025)	+0.008 (−0.023, +0.039)	4/6	0.081 / 0.185
maps, 9 events (top-10% capture)	CNN2D	event year d_0	9	+0.207 (+0.135, +0.278)	+0.210 (+0.105, +0.314)	9/9	—
maps, 9 events (top-10% capture)	CNN2D	placebo	6	+0.002 (−0.014, +0.019)	+0.002 (−0.021, +0.026)	4/6	0.020 / 0.060

Table S17. Sensitivity of the placebo equivalence tests to the margin. The smallest equivalence margin is the margin above which TOST concludes equivalence at $\alpha = 0.05$ ($|\mu| + 1.645 \cdot SE$ for DerSimonian–Laird; $|\mu| + t(0.95, k-1) \cdot SE$ for REML with HKSJ intervals). Prespecified margins: ± 0.01 AUC for point sets and ± 0.02 for map capture. Recomputing the TOST p at the prespecified margins reproduces Table S16 (largest difference 4×10^{-6}).

Point set	Representation / model	k	Pooled placebo (DL; REML)	Smallest equivalence margin, DL	Smallest equivalence margin, HKSJ	TOST p at ±0.005 / ±0.01 / ±0.02 (DL; HKSJ)
AlphaEarth, audit points	point LightGBM	15	+0.002; +0.002	0.0063	0.0074	0.125; 0.174 / 0.001; 0.011 / < 0.001; < 0.001
AlphaEarth, audit points	patch CNN2D	15	−0.002; −0.002	0.0056	0.0059	0.082; 0.093 / < 0.001; 0.002 / < 0.001; < 0.001
TESSERA points	TESSERA, point LightGBM	10	+0.003; +0.003	0.0140	0.0168	0.381; 0.385 / 0.148; 0.184 / 0.006; 0.026
TESSERA points	AlphaEarth, point LightGBM	10	−0.002; −0.003	0.0090	0.0119	0.250; 0.320 / 0.030; 0.089 / < 0.001; 0.004
composite subset points	Sentinel-2, patch CNN2D	13	−0.015; −0.015	0.0338	0.0386	0.821; 0.774 / 0.683; 0.651 / 0.338; 0.360
composite subset points	AlphaEarth, patch CNN2D	13	−0.009; −0.012	0.0218	0.0317	0.720; 0.731 / 0.468; 0.571 / 0.080; 0.242
composite subset points	Sentinel-2, point LightGBM	13	−0.014; −0.014	0.0319	0.0332	0.786; 0.780 / 0.632; 0.631 / 0.285; 0.289
composite subset points	AlphaEarth, point LightGBM	13	−0.005; −0.005	0.0172	0.0184	0.508; 0.508 / 0.254; 0.263 / 0.022; 0.034
maps, events with a placebo (top-10% capture)	point LightGBM	6	+0.007; +0.008	0.0224	0.0325	±0.02: 0.081; 0.185 · ±0.05: < 0.001; 0.009
maps, events with a placebo (top-10% capture)	patch CNN2D	6	+0.002; +0.002	0.0165	0.0213	±0.02: 0.020; 0.060 · ±0.05: < 0.001; 0.002
maps, registered test (5 events)	point LightGBM	5	+0.008	0.0292	—	±0.02: 0.174; — · ±0.05: < 0.001; —
maps, registered test (5 events)	patch CNN2D	5	+0.002	0.0214	—	±0.02: 0.063; — · ±0.05: < 0.001; —

Table S18. Versions of the annual embedding files used. On 16 October 2026 every source file behind the data used was queried with an HTTP HEAD request; all requests returned status 200. Sizes are those of the complete source files, of which only small parts were read. The full lists, with the ETag, size and last-modified date of every file, are Supplementary Data S1 (AlphaEarth) and S2 (TESSERA).

Product	Version and path	Years	Source files	Used for	Last modified (UTC)	Size of the source files
AlphaEarth Satellite Embedding, annual	V1; Source Cooperative `tge-labs/aef/v1/annual`	2017–2025	291 (4,049 blocks read)	all AlphaEarth analyses	2025-11-04 to 2026-03-22	0.84 TB
TESSERA annual representations	v1; Source Cooperative `tessera/tessera/npy/v1`	2017–2025	3,440 (embedding and scale files)	Emilia-Romagna, Fujian, Helene, Jishishan, Luding, Lushan, Mesetas	2026-06-24 to 2026-07-30	232.7 GB
TESSERA annual representations	v1.1-cam; `tessera/tessera/npy/v1.1-cam`	2017–2024	512	Agatha, Freddy, São Paulo; Mesetas (version check)	2026-08-12 to 2026-08-13	40.7 GB

File	SHA-256
AlphaEarth tile index (`aef_index.parquet`, 4 October 2026)	f738e7d274ad582e56e20a3a8b444c6f2a3ece5781f8f9855bb7ca3d9ed2942f
TESSERA manifest v1 (`manifest_v1.parquet`, 14 October 2026)	b7d0717c20f3955b4832ee006aa6d835f18b3a376083f7616205add134246c5a
TESSERA manifest v1.1-cam (`manifest_v1.1-cam.parquet`, 14 October 2026)	3fc630a805a04f9789c07b1248aaf9541122944115abc3ffd99363ff3387c99a
Supplementary Data S1 (AlphaEarth file list)	5f4b94abb832c1f5673c06544dcebac024265f8b71571ee3aa18c50f1e40779d
Supplementary Data S2 (TESSERA file list)	bd8215543029419fb62c3247d8cb27bccc0c7dc4c3d194876a91ec53b95acbb2